



1 **Combination of UAV and terrestrial photogrammetry to assess** 2 **rapid glacier evolution and conditions of glacier hazards**

3 Fugazza, Davide¹; Scaioni, Marco²; Corti, Manuel²; D'Agata, Carlo³; Azzoni, Roberto Sergio³;
4 Cernuschi, Massimo⁴; Smiraglia, Claudio¹; Diolaiuti, Guglielmina Adele³

5 ¹Department of Earth Sciences 'A.Desio', Università degli studi di Milano, 20133 Milano Italy

6 ²Department of Architecture, Built Environment and Construction Engineering, Politecnico di Milano, 20133 Milano Italy

7 ³Department of Environmental science and policy (DESP), Università degli studi di Milano, 20133 Milano Italy

8 ⁴Agricola 2000 S.C.P.A., 20067 Tribiano (MI) Italy

9

10 Correspondence to: Marco Scaioni (marco.scaioni@polimi.it)

11

Abstract

12 Tourists and hikers visiting glaciers all year round face hazards such as the rapid formation of collapses
13 at the terminus, typical of such a dynamically evolving environment. In this study, we analysed potential
14 hazards of the Forni glacier, an important geo-site located in Stelvio Park (Italian Alps), by describing
15 local surface features and evaluating the glacier melting rate. The analyses were based on point clouds
16 and digital elevation models (DEMs) from two separate surveys of the glacier tongue carried out in 2014
17 and 2016 with Unmanned Aerial Vehicles (UAVs), terrestrial photogrammetry (only in 2016) and a DEM
18 obtained in 2007 from an aerial survey. On the area covered by the 2016 survey, average glacier thinning
19 rates of -4.15 m a^{-1} were found in 2007-2016, while the mean thickness change of the glacier tongue in
20 2014-2016 was $-10.40 \pm 2.60 \text{ m}$. UAV-based DEMs were thus found to be sufficiently accurate with
21 respect to the rates of glacier down-wasting, while terrestrial photogrammetry allowed the reconstruction
22 of the glacier terminus, presenting several vertical and sub-vertical surfaces whose modelling was
23 difficult to obtain from airborne UAV images. The integration of UAV and terrestrial photogrammetry
24 provided a detailed and accurate 3D model of the glacier tongue, which we used to identify hazard areas.

25

26 **1 Introduction**

27 The effects of climate change due to global warming are increasingly seen on high mountain regions. In
28 the European Alps, temperatures have increased twice the global average over the last century (Auer et
29 al., 2007; Brunetti et al., 2009). Precipitation patterns show contrasting local trends, with an increase in
30 the northern Alps and a decrease on the southern side (Brunetti et al., 2009), while snow cover has
31 reportedly decreased in the last three decades (Bocchiola and Diolaiuti, 2010; Diolaiuti et al., 2012). The



32 most sensitive indicators of climate change in mountain regions are glaciers and permafrost, both
33 showing unequivocal signs of involution. In the Italian Alps, glaciers have lost at least about a third of
34 their area since the 1950s (Smiraglia et al., 2015). A similar retreat has occurred in the Swiss Alps, where
35 Fischer et al. (2014) report a loss of 28% since 1973, and in the French Alps, with a decrease in glacier
36 area of 25% since the early 1970s (Gardent et al., 2014). Warming trends have also been reported at
37 permafrost monitoring sites throughout Europe, with consequent thickening of the active layer (Harris et
38 al., 2009).

39 Changes to glacier and permafrost environments, either by climate variations alone or in combination
40 with anthropogenic activities, have been recognized to promote land-surface instabilities, playing a
41 significant role in the generation of geomorphological hazards evolving in a downstream direction
42 (Keiler et al., 2010). In glacial and periglacial regions, the most severe hazards are generally related to
43 flooding, through the outburst of moraine- or ice-dammed lakes. Climate change has accelerated the
44 formation of glacial lakes and the expansion of new ones, increasing the risk of devastating glacial lake
45 outburst floods (GLOFs), which frequently occur in the Himalayas, Karakorum, Chilean Patagonia and
46 Peruvian Andes (Wang et al., 2015). In recent years, the formation of moraine-dammed lakes has also
47 been reported in the Swiss Alps, with growing concern of possible overtopping of moraine dams
48 provoked by ice avalanches (Gobiet et al., 2014). Outbursts of water from the englacial or subglacial
49 system are equally threatening: in the French Alps, water-filled cavities were recently identified at
50 Glacier de Tête Rousse, which experienced a deadly rupture of a water pocket in the past (Garambois et
51 al., 2016). Other recurrent hazard situations may arise from ice avalanches from hanging glaciers
52 (Vincent et al., 2015), including the complete detachment of sections of the ice body. In Italy, the partial
53 detachment and fragmentation of the Mount San Matteo serac in Stelvio Park limited spring access to
54 the Forni Glacier for skiers and mountaineers in 2005 and 2006 (Riccardi et al., 2010). More recently,



55 Azzoni et al. (submitted) identified two types of collapse features (see fig. 2) on the tongue of Forni
56 Glacier, namely normal faults and ring faults, both posing serious hazards to mountaineers. The first
57 occur mainly on the medial moraines and are due to gravitational collapse of debris-laden slopes, whereas
58 the latter develop as a series of circular or semicircular fractures with stepwise subsidence, caused by
59 englacial or subglacial meltwater creating voids at the ice-bedrock interface and eventually the collapse
60 of cavity roofs. The retreat and thinning of glaciers in the Alps, while increasing the likeliness of these
61 collapses, is also a major cause of slope instabilities in combination with permafrost thawing, uncovering
62 and debutting rock and debris flanks, increasing mass movement and potentially triggering landslides
63 and rock avalanches (Keiler et al., 2010).

64 **1.1 Remote sensing of glacier hazards**

65 The highly dynamic nature of high mountain environments has led to a widespread use of optical remote
66 sensing for monitoring of glacier-related hazards, with the ability to produce digital elevation models
67 (DEMs) and evaluate changes on the basis of multispectral images. DEMs are particularly useful to detect
68 glacial thickness and volume variations and to identify steep areas that are most prone to
69 geomorphodynamic changes such as mass movements (Blasone et al., 2014). Multispectral images at a
70 sufficient spatial resolution enable the recognition of most glacial- and permafrost-related hazards,
71 including glacier lakes and landslides, their geometric properties and kinematics (Kaab et al., 2005).
72 Indeed, the crucial factors for monitoring of hazard events, which might be localized in small glacial and
73 periglacial areas and evolve over short-time scales, are the revisit time of the sensor and its spatial
74 resolution. In practice, sensors with a high-frequency revisit time often have a coarse spatial resolution
75 (e.g., MODIS), while images from high-resolution optical sensors are costly and with restrictive data
76 access policies (e.g., Pleiades, Worldview). This issue mostly limits data availability to the Landsat
77 TM/OLI family of sensors and Terra ASTER with a maximum spatial resolution of 15 m. Although



78 technological improvements have been made with Sentinel-2, with greater spatial and temporal coverage
79 and finer spectral resolution, cloud cover is still a major issue affecting satellite optical sensors and
80 limiting the acquisition of information over an area of interest. In very recent years, the application of
81 imaging sensors carried by unmanned aerial vehicles (UAVs – Colomina & Molina, 2014, O’Connor et
82 al., 2017) has started to emerge in the glaciological community as a viable low-cost alternative for multi-
83 temporal monitoring of small areas, effectively enabling on-demand research and bridging the gap
84 between field observations, notoriously difficult on glaciers, and coarser resolution satellite data
85 (Bhardwaj et al., 2016a).

86 The use of UAV-based remote sensing for glacier research started in polar environments, in small-scale
87 studies of cryoconite holes (Hodson et al., 2007), and melt ponds (Inoue et al., 2008). During the last
88 decade, UAV photogrammetry (Remondino et al., 2011) has been slowly gaining pace as a tool for the
89 generation of high-resolution DEMs (see, e.g., Rippin et al., 2015). Few studies however have explored
90 the potential of UAVs in high mountain environments, likely due to the following issues:

91

- 92 1. The reduced operating autonomy due to the limited battery support combined with the effects of
93 lower air pressure and temperature;
- 94 2. The complexity of mountainous terrain, which may make it difficult to find suitable take-off and
95 landing sites; and
- 96 3. Potential Problems in the visibility of GNSS (Global Navigation Satellite System) satellites,
97 which can hamper UAV navigation (Bhardwaj et al., 2016a) and may introduce errors in geo-
98 referencing (Santise, 2016).

99



100 Notable exceptions include the works of Immerzeel et al. (2014), who generated a high-resolution
101 orthophoto and DEM to study the dynamics of Lirung Glacier (Nepalese Himalaya) and of Fugazza et
102 al. (2015) in their study of an Alpine glacier. The latter authors produced an orthophoto from a UAV
103 survey and mapped small- and large-scale supraglacial features of the Forni Glacier (Italian Alps),
104 including debris cover, crevasses, epiglacial lakes and the medial moraines, via object-based image
105 analysis (Blaschke, 2010). In Dell'Asta et al. (2017), multiple orthophotos and DEMs were created from
106 UAV data captured over the Gran Sometta rock glacier (Italian Alps); a semi-global matching technique
107 for comparing time-series of both types of raster data was developed in order to detect the surface
108 displacement field. Another technique that has been shown to provide sufficiently accurate point clouds
109 for studying glacier surfaces is terrestrial photogrammetry, although a necessary requirement in this case
110 is that the region of interest must completely observed from ground stations (see, e.g., Piermattei et al.,
111 2015; 2016). An overview of state-of-the-art terrestrial photogrammetry for application in geosciences
112 can be found in James & Robson (2012), Westoby et al. (2012), Smith et al. (2015), and Eltner et al.
113 (2016).

114 In spite of these progresses, an intercomparison of UAV and terrestrial photogrammetry and accuracy
115 evaluation of point clouds is still lacking in glacial environments. While Gindraux et al. (2016) estimated
116 the optimal density of GCPs collected with GNSS sensors to produce accurate DEMs from UAV surveys,
117 comparison against consolidated surveying techniques such as LiDAR (Bhardwaj et al., 2016b) and
118 theodolite measurements is still missing over glaciers.

119 In this study, we focused on a rapidly evolving, hazard-prone glacier in a protected area of the Italian
120 Alps. We compared different platforms and techniques for point cloud, DEM and orthomosaic
121 generation: UAV photogrammetry (from two distinct aircraft), terrestrial (or close-range)
122 photogrammetry (Luhmann et al. 2014) and terrestrial laser scanning (TLS - Vosselman & Maas, 2010),



123 with the aim of: (1) evaluating the accuracy of UAV- and terrestrial photogrammetric products; (2)
124 investigating ice thickness changes on both long and short-time scales; (3) identifying glacier-related
125 hazards, particularly the ones representing acute hazardous phenomena posing risk for mountaineers
126 visiting the glacier during summer.

127 **1.2 Study Area**

128 The Forni Glacier (see Fig. 1a, b), in the Ortles-Cevedale group, was the largest Italian valley glacier
129 (Smiraglia et al., 2015) until 2015, when the easternmost part of its three ice tongues separated from its
130 accumulation basin. The latest Italian Glacier Inventory (based on 2007 data, i.e., before the separation),
131 reported the total glacier area as 11.34 km² (Smiraglia et al., 2015), an altitudinal range between 2501
132 and 3673 m a.s.l. and a North-North-Westerly aspect. The glacier has retreated markedly since the little
133 ice age (LIA), when its area was 17.80 km² (Diolaiuti & Smiraglia, 2010), with an acceleration of the
134 retreating trend in the last three decades (Diolaiuti et al, 2012, D'Agata et al; 2014). It gained scientific
135 importance in 2005, when it was chosen as the site of the first Italian supraglacial automatic weather
136 station (AWS1 Forni, see Citterio et al; 2007), included in the SPICE (Solid Precipitation Inter
137 Comparison Experiment) and CryoNet networks of the WMO (World Meteorological Organization).
138 Recent research on this glacier mainly focused on the modeling of the albedo and debris cover via
139 terrestrial photography (Azzoni et al., 2016), satellite remote sensing (Fugazza et al., 2016), and a UAV
140 survey (Fugazza et al., 2015). Beside its scientific relevance, the main reasons behind the choice of this
141 glacier as a study area are:

- 142 1. The significant retreat of the glacier since the LIA, which sets it as an example of the evolution
143 of valley glaciers in the Alps;
- 144 2. The profound changes in glacier dynamics that have taken place in recent years, including the
145 loss of ice flow from the eastern accumulation basin towards its tongue and the evidence of



146 collapsing areas on the eastern tongue (Azzoni et al., submitted). One such area, hosting a large
147 ring fault (see Fig. 2d) prompted an investigation carried out with Ground Penetrating Radar
148 (GPR) in October 2015, but little evidence of a meltwater pocket was found under the ice surface
149 (Fioletti et al., 2016). Since then, a new ring fault appeared on the central tongue, and the terminus
150 underwent substantial collapse (see Fig. 2a,b,c,e);

151 3. The touristic and mountaineering importance of the site (Garavaglia et al., 2012). In fact, the
152 glacier is included in the list of geosites of Lombardy region (see Diolaiuti and Smiraglia, 2010)
153 and it is located in Stelvio Park, one of Italy's major protected areas. The glacier is frequently
154 visited during both winter and summer months, often by inexperienced hikers unaware of the
155 hazards posed by crevasses and collapsing areas.

156 **2 Data Sources: acquisition and processing**

157 **2.1 2016 surveys**

158 At the end of August 2016, a data acquisition campaign was carried out with the specific aim of
159 reconstructing the glacier tongue of the Forni Glacier. Multiple techniques were adopted and integrated,
160 to evaluate the performances of different approaches and establish a methodology for future repeat
161 surveys. A UAV-photogrammetric survey with a quadcopter (see Sec. 2.1.1) was conducted to provide
162 a DEM of the glacier surface, to be compared with other DEMs dating back to 2007 and 2014. A
163 photogrammetric survey carried out from ground stations (Sec. 2.1.2) was specifically aimed at
164 reconstructing the glacier terminus. In order to assess the quality of the photogrammetric point clouds, a
165 terrestrial laser scanning (TLS) survey of the same area was concurrently conducted (Sec. 2.1.3). In
166 addition, a set of ground control points (GCPs) was measured with GNSS equipment in order to register
167 all the previous point clouds into the mapping frame (Sec. 2.1.4).

168 **2.1.1 UAV Photogrammetry**



169 The UAV survey took place on two separate days, on 30th August and 1st September 2016, during the
170 central hours of the day, as weather conditions on the glacier were rather unstable (rain, excessive cloud
171 cover) and did not allow morning operation or surveying the glacier on consecutive days. Both surveys
172 were carried out under low cloud cover to avoid direct solar radiation on the glacier surface while
173 preserving diffuse illumination conditions (Pepe et al., 2017, submitted). The UAV employed in this
174 survey was a customized quadcopter (see Fig. 3b, Table 1) carrying a Canon Powershot 16 Megapixel
175 digital camera. During experiments prior to the flights on the glacier tongue, it was noticed that the
176 quadcopter drew a significant amount of power for vertical ascension and that it was overly sensitive to
177 vibrations during flight, potentially exposing pictures to motion blur. To deal with the first issue, two
178 different sites were chosen for taking-off and landing. Both places, at elevations above the glacier surface,
179 permitted to gain altitude before take-off and maintain line-of-sight operation with flights at low relative
180 altitude of 50 m, which ensured an average ground sample distance (GSD) of 5.7 cm. The first take-off
181 site was on the eastern lateral moraine (elevation approx. 2700 m a.s.l.), while the second site was a rock
182 outcrop on the hydrographic left flank of the glacier (see Fig. 1b) at an elevation of approx. 2750 m a.s.l.
183 To reduce motion blur, camera shutter speed was set to the lowest possible setting, 1/2000 s, with aperture
184 at F/2.7 and sensitivity at 200 ISO.

185 Several individual parallel flights were conducted to cover a small section of the proglacial plain and
186 different surface types on the glacier surface, including the terminus, a collapsed area on the central
187 tongue, the eastern medial moraine and some debris-covered parts of the eastern tongue. A ‘zig-zag’
188 flying scheme was followed to reduce the flight time. The UAV was flown in autopilot mode using the
189 open-source software Mission Planner (Osborne, 2013) to ensure 70% along-strip overlap and sidelap. In
190 total, two flights were performed during the first survey and three during the second, lasting about 20
191 minutes each. The surveyed area spanned over 0.59 km².



192 Processing of data from the 2016 UAV flight was carried out using Agisoft Photoscan version 1.2.4
193 (www.agisoft.com), implementing a Structure-from-Motion (SfM) algorithm for image orientation (see
194 Barazzetti et al., 2011) followed by a multi-view dense-matching approach for surface reconstruction
195 (Remondino et al., 2014). The availability of GNSS navigation data was exploited to start the SfM
196 procedure, shortening the time necessary to register the 288 images acquired by the quadcopter. No pre-
197 calibration was applied, since the block configuration including strips flown along different directions
198 was optimal for the estimation of camera calibration parameters (Zhang et al., 2017). A total number of
199 38,506 tie points (TPs) were extracted for image orientation, corresponding to an average number of 892
200 TPs per image (see Table 2). The large average number of rays per each TP (6.7) combined with the huge
201 number of TPs offered a sufficient inner reliability for an effective outlier rejection procedure, which is
202 applied during bundle adjustment (Kraus, 1997; Luhmann et al., 2014) in Agisoft Photoscan. This
203 package implements a standard photogrammetric bundle adjustment where GCPs are used as regular
204 weighted observations, unlike most software packages including SfM algorithms where GCPs are only
205 used for estimating a 3D rigid-body transformation for geo-referencing the final point cloud. Eight GCPs
206 (see Fig. 4 and Sec. 2.1.4) were measured for the registration of the photogrammetric blocks and its by-
207 products into the mapping frame. The root mean square error (RMSE) of the GCPs was 40.5 cm, which
208 can be used as an indicator of accuracy for the geo-referencing of the photogrammetric block (see Table
209 2).

210 The point cloud obtained from the 2016 UAV flight was interpolated to produce a grid DEM (see
211 Immerzeel et al., 2014), with a cell resolution of 60 x 60 cm. While the high global point density of the
212 point cloud (89 points/m²) could have permitted a higher spatial resolution, the DEM would have to be
213 subsampled when computing the differences with other grids. This spatial resolution was considered
214 sufficient for the analysis of volumetric changes. An orthoimage was also generated from UAV oriented



215 images and the DEM, with a resolution of 15 cm. Both the DEM and the orthoimage were exported in
216 the ITRS2000 / UTM 32N mapping coordinate frame.

217 **2.1.2 Terrestrial photogrammetry**

218 A terrestrial photogrammetric survey was carried out during the 2016 campaign to reconstruct the
219 topographic surface of the glacier terminus, which presented several vertical and sub-vertical surfaces
220 whose measurement was not possible from the UAV platform in nadir configuration (see Fig. 2e).

221 Images were captured from 134 ground-based stations. Most camera stations were located in front of the
222 glacier, and some on both flanks of the valley in the downstream area, as shown in Fig. 5a. A single-lens-
223 reflex Nikon D700 camera was used, equipped with a 50 mm lens, a full-frame CMOS sensor (36x24
224 mm) composed by 4256x2823 pixels resulting in a square pixel size of 8.4 μm . This photogrammetric
225 block was processed using Agisoft Photoscan version 1.2.4, following a similar pipeline as described in
226 Sec. 2.1.1. In this case, no preliminary information about approximate camera stations was necessary,
227 neither pre-calibration. In such a case, when the photogrammetric block has a sparse geometry (i.e.,
228 images have not been collected along ordered sequences) and no approximate orientation parameters
229 (e.g., camera station from GNSS navigation, as in UAV-photogrammetry) are available, the SfM
230 procedure is applied first on a block of images at down-sampled resolution. This process may provide
231 approximate orientation, limiting the search space for corresponding points in the final SfM, which is
232 applied to full resolution images (Barazzetti et al., 2010).

233 The geometric configuration of the photogrammetric block of the glacier terminus, including hyper-
234 redundant convergent images as well as 90° rolled images, was optimal for the estimation of camera
235 calibration parameters. Seven natural features visible on the glacier front were used as GCPs to be
236 included in the bundle adjustment computation in Agisoft Photoscan. Measurement of GCPs in the field



237 was carried out by means of a high-precision theodolite. The measurement of points previously recorded
238 with a GNSS geodetic receiver (see Sec. 2.1.4) allowed to register the coordinates of GCPs in the
239 mapping frame. The RMSE of 3D residual vectors on GCPs was 34.4 cm, which can be considered as
240 the accuracy of absolute geo-referencing. A very high number (59,157) of tie points (TPs) was found on
241 the images after SfM (see Table 2). In addition, the large mean number of rays per each TP (5.6) resulted
242 in a high reliability of the observations, which mitigates the risk of undetected errors. The final point
243 cloud obtained from the dense matching tool implemented in Agisoft Photoscan covers at a very high
244 spatial resolution the full glacier terminus, with the exception of a few obstructed parts (see Fig. 5b).
245 This part of the Forni glacier has a very complex shape, which evolves at a high dynamic rate. Thus,
246 rather than a quantitative evaluation of the ice bulk, here the main purpose of 3D reconstruction is to
247 allow the morphological analysis of the ice structures and the fracturing and collapsing processes. One
248 working day and two people were required for accomplishing the photogrammetric data acquisition,
249 including operations for measuring GCP coordinates.

250 **2.1.3 Terrestrial Laser Scanning**

251 A long-range terrestrial laser scanner Riegl LMS-Z420i was used to scan the glacier terminus frontally.
252 This instrument works on Time-of-Flight mode (www.riegl.com). One instrumental standpoint located
253 on the hydrographic right flanks of the glacier terminus was established. Issues related to meteorological
254 conditions and to the limited access to unstable areas close to the glacier terminus prevented the operation
255 from a second station on the other flank of the valley. This solution would have resulted in reducing the
256 obstructed areas, as it is usually planned in TLS surveys (see Giussani & Scaioni, 2004). The horizontal
257 and vertical scanning resolution were set up to provide a spatial point density of approx. 5 cm on the ice
258 surface at the terminus. Geo-referencing was accomplished by placing five GCPs consisting in cylinders
259 covered by retroreflective paper (see Scaioni et al., 2004). The coordinates of GCPs were measured by



260 using a precision theodolite following the same procedure adopted for terrestrial photogrammetry.
261 Considering the accuracy of registration and the expected precision of laser point measurement, the
262 global accuracy of 3D points was estimated in the order of ± 7.5 cm. The completion of the TLS survey
263 required half working day, including the time necessary for GCP measurements. A team of four to five
264 people was required for the transportation of the instruments (laser scanner, theodolite, at least two
265 topographic tripods and poles, electric generator and ancillary accessories).

266 **2.1.4 GNSS ground control points**

267 Before the 2016 surveys, eight control targets were placed both outside the glacier and on the glacier
268 tongue (see Fig. 4). Differential GNSS data were acquired at their location for the purpose of accurate
269 geo-referencing of UAV, terrestrial photogrammetry and TLS data. While for geo-referencing of UAV
270 data the GCPs were directly visible on the quadcopter images, for terrestrial photogrammetry and TLS
271 they were adopted for the registration of theodolite measurements (for practical details about standard
272 surveying operations see Schofield & Breach, 2007). The targets consisted in a piece of white fabric 80
273 x 80 cm wide, with a circular marker in red paint chosen to provide contrast against the background.
274 Such GCPs were positioned on stable glacier areas or flat boulders (see Fig. 6).

275 GNSS data were acquired by means of a pair of Leica Geosystems 1200 geodetic receivers working
276 in RTK (Real-Time Kinematics) mode, see Hoffman-Wellenhof (2008). One of them was set up as
277 master on a boulder beside Branca Hut, where a monument had been established to be used as reference
278 point for GNSS surveys in the Forni Glacier region. The coordinates of this point were already known in
279 the geodetic/mapping reference frame ITRS2000 / UTM 32N and were used for geo-referencing all other
280 points measured with GNSS. The second receiver was used as a rover, communicating via radio link
281 with the master station. The maximum distance between master and rover was less than 1.5 km, but the
282 local topography prevented broadcasting the differential corrections in a few zones of the glacier.



283 Unfortunately, no mobile phone services were available and consequently the internet network could not
284 be accessed, precluding the use of the regional GNSS real-time positioning service. The theoretical
285 accuracy of GCPs was estimated in the order of 2-3 cm.

286 **2.2 2014 UAV photogrammetric survey**

287 The first UAV survey conducted over the tongue of Forni Glacier took place on 28th August 2014, using
288 a SwingletCam fixed wing aircraft (see Fig. 3a). This commercial platform developed by SenseFly, with
289 basic technical features reported in Table 1, carries a Canon Ixus 127 HS compact digital camera. The
290 UAV was flown in autopilot mode with a relative flying height of approximately 380 m above the average
291 glacier surface, which resulted in an average GSD of 11.9 cm. The flight plan was organized by using
292 the proprietary software eMotion, by which the aircraft follows predefined waypoints with a nominal
293 along-strip overlap of 70%; sidelap was not regular because of the varying surface topography, but ranged
294 around 60%. Flight operations started at 07:44 AM and ended at 08:22 AM. Early morning operations
295 were preferred as during this time of day the glacier is not yet directly illuminated by the sun, thus diffuse
296 illumination predominates over the glacier surface, and wind speed is at its lowest (Fugazza et al., 2015).
297 These conditions are therefore optimal to avoid saturating the camera pictures due to the high reflectivity
298 of ice surfaces as well as to minimize blurring effects due to the UAV motion. In addition, the presence
299 of tourists on the glacier is reduced during this time of the day. Pictures were automatically captured by
300 the UAV platform, selecting the best combination of sensor aperture ($F=2.7$), sensitivity (between 100
301 and 400 ISO) and shutter speed (between 1/125 s and 1/640 s).

302 Compared to multi-rotor platforms, fixed wing aircraft are capable of longer flight time on glaciers, due
303 to their simple structure and the ability to exploit aerodynamics to take advantage of gliding and reduce
304 battery consumption (Bhardwaj et al., 2016a). This allowed covering an area of 2.21 km² in just two



305 flight campaigns, with a low altitude take-off (lake Rosole, close to Branca Hut, see Fig. 1b). Both the
306 terminal parts of the central and eastern ablation tongue were surveyed. The considerable difference in
307 area covered during the 2014 and 2016 surveys is due to the reduced battery life of the quadcopter and
308 lower flying height throughout the 2016 survey.

309 Processing of data from the 2014 UAV flight was carried out using Agisoft Photoscan version 1.2.4 in a
310 similar approach to the one applied for UAV-photogrammetry data collected in 2016. Since no GCPs
311 were measured during the 2014 campaign, the registration of this data set into the mapping frame was
312 based on GNSS navigation data only. Consequently, a global bias in the order of 1.5-2 m resulted after
313 geo-referencing, and no control on the intrinsic geometric block stability could be possible. After the
314 generation of the point cloud, a DEM and orthoimage were produced following the methods outlined in
315 Sec. 2.1.1, with the same spatial resolutions of final products of 60 cm and 15 cm, respectively.

316 **2.3 2007 DEM**

317 The 2007 TerraItaly DEM was produced by BLOM C.G.R (Compagnia Generale Riprese Aeree) for
318 Lombardy region. It is the final product of an aerial survey over the entire region, that was conducted
319 with a multispectral pushbroom Leica ADS40 sensor acquiring images from a flying height of 6,300 m
320 with an average GSD of 65 cm. The images were processed to generate a DEM with a cell resolution of
321 2 m x 2 m, and projected in the former national ‘Gauss Boaga - Fuso I’ coordinate system based on the
322 Monte Mario datum (Mugnier, 2005). Heights were converted from ellipsoidal to geodetic using the
323 official software for datum transformation in Italy (Verto ver. 3), which is distributed by the Italian
324 Geographic Military Institute (IGMI). The final vertical accuracy reported by BLOM C.G.R. is ± 3 m.
325 The only processing step performed within this study was the datum conversion to ITRS2000, using a
326 seven-parameter similarity transformation based on a local parameter set provided by IGMI.



327 **2.4 DEM co-registration**

328 Several studies have found that errors in individual DEMs, both in the horizontal and vertical domain,
329 propagate when calculating their difference leading to inaccurate estimations of thickness and volume
330 change (Berthier et al., 2007; Nuth & Kaab, 2011). In the present study, different approaches were
331 adopted for geo-referencing all the DEMs (2007, 2014, 2016) used in the analysis of the volume change
332 of the Forni Glacier tongue. The 2007 DEM was extracted from a regional data set, which required a
333 transformation from the old datum ‘Gauss-Boaga - Fuso I’ to the present datum ITRS2000/UTM 32 N.
334 This transformation has an absolute positional accuracy at cartographic level in the order of 1-2 m,
335 depending on the zone. The DEM obtained from 2014 UAV campaign was geo-referenced on the basis
336 of onboard GNSS navigation data, with an accuracy with respect to the above mentioned mapping datum
337 in the order of 1.5-2 m. On the other hand, the most recent DEM derived from the UAV flight (2016)
338 was geo-referenced using a set of GCPs measured with geodetic-grade GNSS receivers. The average 3D
339 residuals of these GCPs, which is in the order of 40.5 cm, can provide an estimate of the global geo-
340 referencing accuracy of the 2016 data set.

341 To compute the relative differences between the DEMs, a preliminary co-registration was therefore
342 required. The method proposed by Berthier et al. (2007) for the co-registration of two DEMS was
343 separately applied to each DEM pair (2007-2014; 2007-2016; 2014-2016). Following this method, in
344 each pair one DEM plays as reference (‘master’), while the other is used as ‘slave’ DEM to be iteratively
345 shifted along x and y directions by fractions of pixel to minimize the standard deviation of elevation
346 differences with respect to the ‘master’ DEM. Only areas assumed to be stable are considered in the
347 calculation of the co-registration shift. The ice-covered areas were excluded by overlaying the glacier
348 outlines from D’Agata et al. (2014) for 2007 and Fugazza et al. (2015) for 2014. The oldest DEM, which
349 is also the widest in each comparison, was always set as the master. To co-register the 2014 and 2016



350 DEMs with the 2007 DEM, both were resampled to 2 m spatial resolution, whereas the comparison
351 between 2014 and 2016 was carried out at the original resolution of these data sets (60 cm).

352 All points resulting in elevation differences larger than 15 m were labelled as unreliable, and
353 consequently discarded from the subsequent analysis. Such larger discrepancies may denote errors in one
354 of the DEMs or unstable areas outside the glacier. Values exceeding this threshold however were only
355 found in a marginal area with low image overlap in the comparison between the 2014 and 2016 DEMs,
356 with a maximum elevation difference of 36 m. Once the final co-registration shifts were computed (see
357 Table 3), the coefficients were subtracted from the top left coordinates of the ‘slave’ DEM; the residual
358 mean elevation difference was also subtracted from the ‘slave’ DEM to bring the mean to zero.

359 **3 Results**

360 **3.1 Comparison between observations from 2016: UAV/terrestrial photogrammetry and TLS**

361 The comparison between data sets collected during the 2016 campaign had the aim of assessing the
362 quality of different data sources to be used for subsequent physical analyses. In addition, these
363 evaluations were expected to provide some guidelines for the organization of future investigations in the
364 field at the Forni Glacier and in other Alpine sites.

365 Specifically, in this case the analysis consists in comparing point clouds. It is out of the scope of this
366 article to address this topic in an exhaustive manner. While the reader may refer to other pieces of
367 literature to have a broader view about it (e.g., Eltner et al., 2016), here the aim is to apply some existing
368 criteria and metrics to find out which techniques among UAV photogrammetry (i), terrestrial
369 photogrammetry (ii), and TLS (iii) should be privileged for glaciological studies under certain conditions.
370 Of course, comparing two point clouds, which is the simplest case that may be considered, is more
371 complex than comparing coordinates of specific points that have been measured, e.g., with theodolites,



372 GNSS sensors or target-based photogrammetry (Luhmann et al., 2014). In such a case, the analysis is
373 limited to evaluating their discrepancies by merely differencing corresponding coordinates, provided that
374 the points to compare are defined into the same reference frame. The maximum degree of complexity in
375 the case of specific point comparison is to define the minimum departure revealing statistical significance
376 (Teunissen, 2009). In the case of point clouds, no precise point-to-point correspondence generally exists,
377 since 3D points are obtained using different techniques, setups and algorithms. In addition, not only the
378 ‘distance’ between point clouds should be assessed to check out their spatial accuracy, but other
379 properties need to be considered as well. In particular, point density and completeness of a point cloud
380 are two important aspects that in general do not deserve consideration when dealing with specific points.
381 Thus a first important property to analyse is the point density, which allows verifying whether the whole
382 reconstructed surface may be modelled with sufficient detail on the basis of the surveyed point cloud. Of
383 course, the same point density may be fine for a certain kind of geomorphometry, whilst it may not be
384 sufficient for others, mainly depending on roughness. Secondly, the completeness of a reconstruction
385 indicates if the surface reconstruction presents some holes or missing parts, for example because of
386 occlusions, sensor out-of-range areas, low-texture or low-reflectivity surfaces, and the like. Eventually,
387 the accuracy of a point cloud should be assessed by comparison with a reference surface or with a set of
388 precise points. Different criteria exist for evaluating the spatial ‘distance’ between two point clouds (see
389 Lindenbergh and Pietrzyk, 2015; Scaioni et al., 2015), depending on the surface morphology, as
390 described at paragraph 3.1.2.

391 In order to analyse point density, completeness and accuracy of point clouds obtained during 2016
392 campaign by means of techniques (i), (ii) and (iii), five regions shown in Fig. 7 were selected. These
393 regions are mainly located on the glacier and characterized by different geomorphological properties. In
394 addition, they were surveyed by almost all the three techniques. The analysis of local regions was



395 preferred to the analysis of the entire point clouds for two reasons: (1) the partial overlap between point
396 clouds obtained from different methods; (2) the opportunity to investigate the performances of the
397 techniques in diverse geomorphological situations.

398 A short description of each sample window follows:

- 399 1. Glacial cavity located on the right orographic side of the glacier terminus, composed by sub-
400 vertical and fractured surfaces over 20 m high, and forming a typical semi-circular shape (clearly
401 visible from the top);
- 402 2. Glacial cavity located on the left orographic side of the glacier terminus. It is over 10 m high with
403 the typical semi-circular shape as window 1; on top, it is covered by fine- and medium-size rock
404 debris;
- 405 3. Vertical fault on the left orographic flank of the glacier terminus, over 10 m high;
- 406 4. Highly-collapsed area on the central region of the glacier terminus, covered by fine- and medium-
407 size rock debris and rock boulders; and
- 408 5. Planar surface with a vertical fault on the left orographic side of the glacier terminus, covered by
409 fine- and medium-size rock debris and rock boulders.

410 Table 4 reports the size of each sample window as well as the number of points obtained with different
411 techniques. In window 1, method (i) could not provide points except on the upper part, because of the
412 presence of sub-vertical cliffs that could not be reconstructed from airborne images. Window 5 was not
413 covered by TLS (iii), because it was not included in the field-of-view of the selected standpoint. Looking
414 at the point number in each window, at a first glance terrestrial photogrammetry resulted in a much
415 consistent data set than other techniques. This is mostly motivated by the flexibility of this methodology,
416 which allows carrying out data acquisition from multiple stations, depending only on the terrain
417 accessibility in front of the glacier.



418 **3.1.1 Point density and completeness**

419 Point density describes the number of points per unit of surface or volume. Depending on the adopted
420 surveying techniques, it always depends upon the distance between sensor and surface and the adopted
421 spatial resolution. While in the UAV-photogrammetry survey the distance camera-object is almost
422 constant (approx. 180 m) in all sample windows, in the case of terrestrial sensors (TLS &
423 photogrammetry) this distance is greater and therefore it can influence the point cloud reconstruction. In
424 the terrestrial photogrammetry survey, the distances between camera stations and the sample windows
425 ranged from 85 m (window 2) to 137 m (windows 1, 3 and 4), and 206 m (window 5).

426 In the case of photogrammetry the point cloud reconstruction relies on dense matching, thus the resulting
427 point density also depends upon the surface texture.

428 The evaluation of point density using a global descriptor that is applied to the whole point cloud or on
429 large portions of it cannot provide a useful output in the case of glaciers with complex morphology, since
430 point density may largely change from one portion of surface to another. More significant is the use of
431 local descriptors applied on small windows or in the proximity of each point. Local results can be
432 displayed on maps and summarized by global statistics.

433 In this study, the number of neighbours N (inside a sphere of radius $R=1$ meter) divided by the
434 neighbourhood surface was used to evaluate the local point density D :

$$435 \quad D = \frac{N}{\pi * R^2} \quad (1)$$

436 This function is implemented in the open-source software CloudCompare (www.cloudcompare.org).

437 Point cloud completeness refers to the presence of enough points to completely describe a portion of
438 surface. A rigorous evaluation of this parameter is possible by interpolating a regular surface and by
439 searching for the presence of points in any sectors of it. Of course, this approach can be easily applied



440 when the morphology of the surface to reconstruct is regular, for example in the analysis of terrain
441 topography. On the other hand, in the case of an Alpine glacier terminus, the geometry is much more
442 complex, and the recourse to this approach is more difficult. Consequently, in this study a heuristic
443 evaluation based on the visual inspection of the obtained windows was preferred.

444 Mean values and standard deviations of point density in the five windows are shown in Table 5 and Fig.
445 8. The following general considerations can be made. The values of point density obtained from
446 terrestrial photogrammetry (ii) are much higher than others, except in window 5 that features a gentle
447 slope. In such a case, UAV photogrammetry provided results comparable to the ones of terrestrial
448 photogrammetry (only approximately three times smaller). On the other hand, the mean point density
449 achieved when using technique (ii) has a large variability both between different windows, and inside
450 each window as witnessed by the standard deviations of D . Point densities related to UAV
451 photogrammetry (i) and TLS (iii) are more regular and constant. In case (i), the regularity is due to the
452 structure of the airborne photogrammetric block, which is made up of organized parallel strips looking
453 in nadir direction towards the ground. In case (iii), the regularity is motivated by the constant angular
454 resolution adopted during scanning. In general, each sensor performs better when the surface is
455 orthogonal to the average sensor looking direction. Mainly, this means that terrestrial techniques (ii) and
456 (iii) perform better in vertical and sub-vertical cliffs (windows 1 and 2), and in high-sloped surfaces
457 (windows 3 and 4); on the contrary, UAV photogrammetry provided the best results in the case of
458 window 5 that is less inclined and consequently could be well depicted in nadir photos.

459 In term of absolute values, the mean point density obtained with different techniques in the sample
460 windows may suffice for a correct representation of the glacier outer surfaces and the surrounding terrain.
461 In order to understand the effect of point density dispersion, the standard deviations were considered.
462 Since the normal distribution of the data sets made up of point density computed inside each sample



463 window cannot be proved, an approach based on the use of Chebichev theorem was applied (see
464 Teunissen, 2009). Based on this theorem, given a population of N members with mean μ and standard
465 deviation σ , the minimum frequency of the elements comprehended in the interval $\mu \pm 2\sigma$ is 75%. This
466 means that in both queues, 25% of the population can be found. Since the inferior part of the population
467 of point density may be too low to guarantee a detailed modelling of the surface, the upper limit
468 corresponding to the inferior 12.5% percentile was computed and reported in Table 5.

469 Based on the mere analysis of point density, terrestrial photogrammetry outperformed other techniques.
470 In windows 1-4, mean values of this parameter ranged between 1384-2297 points/m², which are
471 equivalent to a range between approximately 14-23 points/dm². A lower point density was obtained in
472 window 5 that is exposed upwards, with approximately 500 points/m². Looking at the limit of the inferior
473 12.5% percentile, three windows (1-3) show a very high value between 766-880 points/m², while in
474 window 5 a value of 31 points/m² was obtained. All these values were retained sufficient for the
475 reconstruction of different surfaces in the sample windows, according to their different geomorphic
476 complexity, except in the case of window 5.

477 In the case of UAV photogrammetry (i), similar results about point density were found in all sample
478 windows, especially for the standard deviations that were always in the range 22-29 points/m². Mean
479 values were between 103-109 points/m² in windows 2-4, while they were higher in window 5 (141
480 points/m²). Due to the nadir acquisition points, the reconstruction of vertical/sub-vertical cliffs in window
481 1 was not possible. The limit of the inferior 12.5% percentile was between 49-62 points/m² because of
482 sub-vertical orientation of this sample window. A higher value (97 points/m²) was found in the case of
483 window 5. Results obtained from photogrammetry based on terrestrial and UAV platforms may be
484 retained quite complementary: the former are suitable for the reconstruction of vertically oriented
485 regions, the latter for those surfaces looking upwards.



486 More varying results were obtained from the use of TLS. With the only exception of window 5, where
487 no sufficient data were recorded due to the position of this region with respect to the instrumental
488 standpoint, a mean value of point density ranging from 141-391 points/m² could be found. Standard
489 deviations ranged between 69-217 points/m², moderately correlated with respective mean values. On the
490 other hand, in correspondence of the inferior 12.5% percentile, too low values were found (0-29
491 points/m²). These results showed that the adopted long-range TLS instrument was not completely
492 suitable for surveying the glacier terminus.

493 In Fig. 9 and 10, the maps of point density in windows 2 and 3 are shown, respectively. These windows
494 depict some typical problems related to the completeness of surface reconstruction that may be obtained
495 from the adopted techniques. UAV photogrammetry can provide a sufficient point density in all parts of
496 those regions that are exposed upwards, as can be seen also in the global model of the glacier shown in
497 Fig. 12. Results are also satisfying in gently sloped areas, as it can be observed in windows 2 and 3, see
498 Fig. 9 and 10. Vertical and sub-vertical surfaces cannot be investigated, requiring the integration with a
499 terrestrial sensor or the installation of the payload camera in oblique configuration.

500 Terrestrial photogrammetry offers the chance to gather images from several positions. This results in
501 reducing the effect of occlusions with a consequently more complete reconstruction. On the other hand,
502 this technique is limited when the surface to reconstruct is close to the horizontal orientation. In such a
503 case, the integration with UAV data is required.

504 In general, TLS suffers from occlusions as all 3D measurement techniques (see for example results in
505 window 2 in Fig. 9). Besides, these instruments are still quite complex to be carried and setup. These
506 limits prevent the acquisition from several viewpoints as it is possible when using photogrammetry. Data
507 acquisition is also difficult in regions that are close to be parallel to the laser beams and in the presence
508 of wet surfaces. Another problem with the adopted TLS concerned the angular resolution adopted for



509 scanning, which was set up to obtain a linear resolution on the ground surface of approximately 1 point
510 every 5 cm, while keeping the acquisition time at about 40 minutes. Using a smaller angular resolution
511 would have resulted in much longer acquisition time (for example, using half resolution could be possible
512 in four times the acquisition time). On the other hand, the adopted laser scanner instrument still has a
513 slow acquisition speed (approx. 12 kHz) if compared with up-to-date Time-of-Flight lasers which may
514 work much faster (over 100 kHz).

515 Finally, internal parts of fractures and faults are usually problematic to reconstruct by means of all
516 measurement techniques. However, their presence can be easily detected in the point clouds.

517 **3.1.2 Accuracy**

518 The evaluation of the accuracy of a point cloud requires a data set of benchmarking observations. When
519 the geometry of an object is known a priori (for example a planar surface), the accuracy can be evaluated
520 by comparing the point cloud to the mathematical model of the surface itself. On the other hand, in the
521 case of terrain or glacier geomorphology, this solution is clearly not viable. In such a case, benchmarking
522 data are required, for example, another reference point cloud or a set of specific points (see Eltner et al.,
523 2016). Due to the fast dynamics of the glacier tongue under investigation, the only available data sets to
524 compare are the ones collected during the 2016 campaign, i.e., point clouds derived from UAV and
525 terrestrial photogrammetry, and from TLS. The approach applied to estimate the accuracy was to
526 compare in a pairwise manner the point clouds obtained from different surveying techniques. The
527 analysis was carried out inside the same five sample windows used for investigating the point cloud
528 density. Although each point cloud had been already geo-referenced as described in Section 2, some
529 residual errors could be expected. In order to get rid of these discrepancies that would affect both surfaces
530 to compare, a preliminary co-registration using the ICP algorithm (Pomerleau et al., 2016) was
531 conducted. Secondly, point clouds in corresponding sample windows were compared using M3C2



532 algorithm implemented in CloudCompare (Lague et al., 2013). The advantage of this algorithm is that it
533 is able to provide a map of signed distances between corresponding and co-registered point clouds. The
534 positive direction of distances goes outside the ‘reference’ point cloud. Therefore, when a computed
535 M3C2 distance is positive, the compared (‘slave’) point cloud lies outside with respect to the reference
536 point cloud. Unlike standard algorithm for comparing DEMs that operate along a predefined direction
537 (see, e.g., Scaioni et al., 2013), here the direction of distance depends on the local normal to the point
538 cloud. This method is therefore suitable to compare complex point clouds such as the ones in the sample
539 windows. The point cloud collected using TLS was used as reference, since these measurement sets were
540 retained to be the most accurate, although their point density and completeness may not be the best ones
541 as proved in the previous section. When comparing both photogrammetric data sets, the one obtained
542 from UAV was used as reference because of the even distribution of point density within the sample
543 windows.

544 Table 6 reports some statistics on the computed M3C2 distances in terms of mean values and standard
545 deviations. Where no data are shown, the comparison was not possible since one or both point clouds
546 were incomplete (for example, in the case of data sets in windows 1 and 5). The comparison between
547 TLS and terrestrial photogrammetry resulted in a high similarity between the accuracy of both point
548 clouds, provided that the TLS point cloud may be assumed as benchmarking surface. No large departures
549 were found between results obtained in different sample windows. In addition, the RMSE are in the order
550 of theoretical precision achievable with photogrammetry techniques under the actual acquisition
551 geometry (Luhmann et al., 2014). This result confirms the small differences between point clouds.
552 Nevertheless, this analysis was carried out after a posteriori ICP-based registration that may have fixed
553 residual geo-referencing errors. By looking at the residuals on GCPs for TLS and terrestrial
554 photogrammetry (7.5 cm and 34.4 cm, respectively) a bias larger than the RMSE found for the distances



555 in different windows were obtained for the latter. Indeed, the identification of natural GCPs on the glacier
556 surface was quite difficult and resulted in low-precision measurements. A solution to improve the quality
557 of geo-referencing in the photogrammetric block should be considered, for example by directly
558 measuring a part of the photo-stations as proposed in Forlani et al. (2014), instead of recurring to GCPs
559 on the glacier surface.

560 The comparison between TLS and UAV photogrammetry provided significantly worse results that may
561 be summarized by the RMSEs in the range 21.1-37.7. These departures may be attributed to two main
562 reasons: (1) these techniques offer the best performances in opposite situations: flat terrain in the case of
563 a UAV survey and vertical surfaces in the case of TLS; (2) the UAV flight was geo-referenced on a set
564 of GCPs obtaining a RMSE of residuals of 40.5 cm, thus the ICP co-registration may have not totally
565 compensated the existing bias.

566 The comparison between UAV (assumed as reference) and terrestrial photogrammetry provided similar
567 results to the ones obtained in the previous analysis. Indeed, the same reasons may still hold in such a
568 case, since two point clouds obtained from ground-based and airborne camera poses were compared.
569 This makes it possible to fuse both point clouds from photogrammetry to obtain a complete model of the
570 glacier tongue, as reported in Sec. 3.3.

571 **3.2 Glacier Thickness change 2007-2016**

572 After DEM co-registration, the resulting shifts reported in Table 3 were applied to each 'slave' DEM,
573 including the entire glacier area. Then the elevations of the 'slave' DEM were subtracted from the
574 corresponding elevations of the 'master' DEM to obtain the Δ DEM. Each Δ DEM was then clipped within
575 the glacier outlines to provide pairwise relative estimates of glacier elevation change. First this operation
576 was carried out by considering the largest possible area in each Δ DEM (see Fig. 11 and Table 7), using



577 the oldest outlines available. This operation was aimed at investigating ice lost in areas of glacier retreat.
578 Secondly, a minimum extension common to all three DEMs was analysed as a means of independently
579 checking the quality of each surface and finding thinning trends over a reference area. Indeed, while the
580 2007 aerial DEM covers the entire Lombardy region, the coverage of both UAV DEMs (2014 and 2016)
581 is limited. Although the DEM from 2016 has the smallest extent, it is not completely included within the
582 extension of 2014 DEM. In practice, however, the reference area almost completely refers to the extent
583 of the 2014-2016 analysis, covering 0.32 km². For the second comparison, the volume change over the
584 glacier tongue and its uncertainty were estimated as well. The method proposed in Howat et al. (2008)
585 was applied, which expresses the uncertainty of volume change as the combination of the standard
586 deviation computed from the residual elevation difference over stable areas, and the truncation error
587 implicit when substituting the integral in volume calculation with a finite sum, according to Jokinen and
588 Geist (2010).

589 When comparing over the maximum possible glacier extension, the latter appears clearly inversely
590 related to the thinning rates. However, the comparison between 2007 and 2014 includes sections of the
591 central tongue that only lost an average 15 m of ice. Considering a common reference area, an
592 acceleration of glacier thinning seems to have occurred over recent years over the lower glacier tongue,
593 from -4.55 in 2007-2014 to 5.20 ma⁻¹ in 2014-2016 (see Table 8).

594 The eastern ablation tongue appears the most affected by glacier thinning between 2007 and 2014, with
595 ice thickness changes persistently below -30 m over the period and between -40/-50 m between 2014
596 and 2016. The greatest ice loss between 2007 and 2014 occurs in correspondence with local collapse of
597 ice cavities, localized in small areas of the eastern tongue (see Fig. 11a), with local thinning generally
598 above -50 m and a maximum of -66.80 m. Conversely, between 2014 and 2016 glacier thinning is close
599 to the mean of approximately 10 m on both the central and eastern sections of the tongue. Only in areas



600 of local collapse is this value greatly exceeded, with a maximum of -38.71 m thinning at the terminus
601 and local maxima above -25 m on the medial moraine and left margin of the central tongue (see Fig.
602 11c).

603 **3.3 Data fusion of point clouds from UAV and terrestrial photogrammetry**

604 As shown in the previous analysis, data sets obtained from ground-based and UAV photogrammetry are
605 quite complementary. In order to derive a full 3D model of the terminal part of the tongue of Forni
606 Glacier, point clouds were fused together. The merged point cloud was subsampled to keep a minimum
607 distance between adjacent points of 20 cm (see Fig. 12). The size of this point cloud was approximately
608 4.4 million points. RGB information from photogrammetric data sets were used for colouring the point
609 clouds before data fusion. The merged point cloud was used for the analysis of glacier hazards and risks
610 reported in Sec. 4.2.

611 **4 Discussion**

612 **4.1 Evolution of the glacier tongue**

613 The outcomes of the DEM differencing procedure indicate generalized thinning of the Forni Glacier
614 tongue over the entire study period. Independent validation of the thinning rates found in this study is
615 available from Senese et al. (2012), who estimated the specific mass balance at the glacier AWS between
616 2006 and 2009, by calculating ablation via the glacier energy budget and accumulation via a sonic ranger.
617 The authors reported a mean annual mass balance of -4.70 m w.e. between 2005 and 2009, with minimum
618 negative of -4.20 and maximum negative of -4.90 m w.e. In comparison, by calculating the geodetic mass
619 balance using the mean ice density of 0.917 g/cm^3 , we found mean annual values of $-4.17 \pm 0.22 \text{ m w.e.}$
620 between 2007 and 2014 and -4.36 ± 0.27 between 2007 and 2016 over the lower part of the glacier
621 tongue, slightly lower but encompassing a wider spatial and temporal range. Besides, our data suggests
622 that thinning over the last two years was higher than between 2007 and 2014.



623 Although thinning rates are high over the entire tongue, they are not homogeneous, and both the glacier
624 preexisting surface morphology and debris input from the valley walls (Azzoni et al., under revision)
625 played an active role in determining the evolution of the glacier tongue that we identified by means of
626 elevation transects on the three DEM surfaces. In particular, the ice-cored medial moraines changed
627 dramatically. In 1987, they were 12 m tall and 50 m wide at maximum on the glacier tongue (Smiraglia,
628 1989), but both width and height gradually increased over the years: the eastern moraine is the more
629 prominent of the two, widening asymmetrically towards the terminus, with the left flank being the widest
630 (see Fig. 13). Along of the middle transect, the height of the eastern moraine remained stable at 15 m
631 between 2007 and 2016, while its width increased from 80 to 100 m. During this period, a new moraine
632 also formed on the eastern tongue, reaching a height of approximately 7 m in 2016. East of this newly
633 formed moraine, ice thinning was above 60 m between 2007 and 2016, likely due to the reduction of
634 mass input from the eastern icefall and the development of a thin debris cover promoting ice ablation
635 (see Fig. 13, middle transect).

636 Further upvalley, as a result of differential ablation, thinning was lower on the medial moraine than on
637 the exposed ice surface. Thus, the height of the eastern moraine increased from 20 to approximately 26
638 m between 2007 and 2016, while its width went from 100 to 145 m. A small new moraine developed,
639 joining the main one in SE-NW direction. The most prominent feature on the central tongue is however
640 the large collapse at the left margin, with 26 m ice thinning between 2014 and 2016 (Fig. 13, bottom
641 transect). At the terminus, the height of the eastern medial moraine decreased between 2007, when it was
642 about 20 m tall, and 2016, when it was approximately 13 m, due to the development of normal faults
643 subparallel to the main medial moraine direction. Conversely, its width gradually increased from 100 to
644 130 m in 2016. The glacier surface once flat is now increasingly hummocky both on the central and
645 eastern sections of the tongue (see Fig. 13 top transect).



646 **4.2 Glacier-related hazards and risks**

647 The collapse of sections of the glacier appears to pose the most significant risk to mountaineers. Collapses
648 are more dangerous than crevasses because of the larger size and relief involved. Besides, already
649 collapsed areas could be filled with snow and rendered entirely or partly invisible to mountaineers.
650 Currently, hikers heading to Mount San Matteo during the summer take the trail crossing the Forni
651 Glacier on the central tongue, dangerously close to the collapsing glacier terminus. During wintertime,
652 ski-mountaineers instead access the glacier from the eastern side, crossing the medial moraine and
653 potentially collapsed areas there (see Fig. 14).

654 While most collapsed areas on the glacier tongue are in fact normal faults, two large ring fault systems
655 can be identified: the first, located on the eastern section (see Fig. 2d and 15a), covered an area of
656 $25.6 \times 10^3 \text{ m}^2$ and showed surface lowering of up to 5 m in 2014. This area was not surveyed in 2016,
657 since field observation did not show evidence of further subsidence. Conversely, the ring fault that only
658 emerged as a few semi-circular fractures in 2014 grew until cavity collapse, with a vertical displacement
659 up to 20 m and further fractures extending south-eastward (see Fig. 2c and 15b), thus potentially widening
660 the extent of collapse in the future. As regards normal faults, those on the eastern moraine developed
661 rapidly in the vertical domain reaching a relief of 12 m in 2016. The collapse was even more rapid at the
662 terminus, leading to the formation of three sub-vertical facies, which could not be analyzed by UAV data
663 alone given the nadir image acquisition. Here, integration of close-range photogrammetry proved
664 necessary to investigate the cliff height, which reaches up to 24 m, while the height of the vault is as low
665 as 10 m. The fast retreat pace of this glacier suggest the terminus will recede along the fault system on
666 the eastern moraine, increasing the occurrence of hazardous phenomena in this area where the
667 vulnerability (occurrence of paths followed by mountaineers) is relatively high, thus making glacier risk
668 particularly significant here. Upvalley, the increased relief of the medial moraine might cause more
669 frequent landslides and rockfalls, which can be dangerous for mountaineers during the summer season.



670 Finally, the collapse of the glacier tongue at its margins will further compromise access to the glacier for
671 winter activities.

672 In these fragile and dynamic areas, the combination of UAV and terrestrial surveys potentially allows
673 following the evolution of glacial hazards (e.g., ring faults, collapsed zones, glacier sectors with a very
674 thin ice layer, etc.) over a summer season or with a higher time frequency than previously possible. This
675 information will be crucial to manage the vulnerability of the area and thus reduce the level of risk. In
676 fact, based on the orthophotos obtained from UAV surveys, it will be possible to identify safer paths
677 where mountaineers and skiers can visit the glacier and reach the most important summits (e.g., Mount
678 San Matteo, etc..) without crossing the most dangerous zones. These safer paths will be identified with
679 the help of local alpine guides and reported in the webpage of the Stelvio National Park and in the
680 Geoportale of the Lombardy Region, to increase the number of citizens potentially visiting the area who
681 will be informed about the dangers and the safest paths. Our surveys also helped describe new categories
682 of glacier hazards and risk (for a review see RGSL, 2003), such as faults and ring faults, which were not
683 considered in the guidelines for the management of environmental risk in the past. Their recent
684 emergence, driven by the present climate change and the subsequent glacier downwasting, requires a
685 new approach to risk management. In this context, it is at present impossible to reduce the glacier hazards
686 and the only chance to lower the risk level is to reduce the vulnerability by changing the tourist paths to
687 safer areas, only possible by applying UAV and terrestrial photogrammetry-based monitoring.

688 **5 Conclusions**

689 In our study, we assessed the potential of UAV and terrestrial photogrammetry to map surface features
690 pertaining to the collapse of a large Alpine glacier (Forni Glacier, Italian Alps), such as ring faults,
691 representing hazards for mountaineers, and reconstruct the thickness changes and variations in
692 topography. We assessed the accuracy of surface elevations by comparing point clouds from UAV and



693 terrestrial photogrammetry against those obtained from TLS and by measuring DEM differences from
694 repeat UAV surveys on stable areas.

695 By comparing different DEMs of the glacier tongue, we found an increased rate of glacier ablation in
696 recent years, reaching $5.20 \pm 1.11 \text{ ma}^{-1}$ between 2014 and 2016, with a maximum surface elevation
697 change of -38.71 m . At the same time, the eastern medial moraine and terminus underwent major
698 changes: the first widened and increased in relief, while also experiencing several faults; the second
699 experienced relevant collapses while the glacier surface became increasingly hummocky. We combined
700 point clouds obtained from UAV- and terrestrial photogrammetry to investigate the hazards on the glacier
701 tongue and the risk to mountaineers and skiers following routes to the popular summits of the area. The
702 glacier terminus is at present the most dangerous area, because it hosts vertical cliffs with a relief up to
703 24 m and it is the main gateway to the glacier during the summer. Collapses at the margins of the central
704 tongue also increase the risk for skiers during winter. The scenario of present glacier downwasting,
705 besides potentially increasing mass movements from currently unstable slopes, might further
706 compromise the access to Forni Glacier in the future, modifying the surface topography and increasing
707 the occurrence of collapses.

708 Our results also show that a sufficient level of accuracy can be achieved by using UAVs to monitor the
709 glacier topographic changes over yearly timescales, as the variations that take place are larger than the
710 associated uncertainty. Thus, UAV surveys could be used effectively to investigate the glacier
711 downwasting. The integration with terrestrial photogrammetry is crucial to establish a valid alternative
712 to TLS to monitor recurrent glacier hazards with larger impact on downstream populations, allowing the
713 estimation of volumes involved in the detachment of seracs or hanging glaciers, and measurements of
714 the height of moraine dams to help manage potential GLOFs. Terrestrial photogrammetry may provide
715 better results than TLS in term of point density and point cloud completeness, thanks to the chance to



716 capture images from a high number of camera stations, limiting occlusions. When analyzing the point
717 cloud accuracy, the comparison of photogrammetric outputs with respect to TLS outputs revealed
718 average discrepancies in the order of a few centimeters in the case of terrestrial blocks, and a few
719 decimeters in the case of UAV blocks. This result, although quite promising, is not yet sufficient for
720 monitoring of intra-seasonal variations of the glacier topography, or very rapid changes occurring on
721 daily timescales such as those involved in the collapse of ice blocks at the terminus. Beside the
722 combination with terrestrial photogrammetry, improvements to our UAV survey design might include a
723 greater number of GCPs sampled in a dense spatial network, but the glacier dynamics evolving towards
724 a collapse scenario might make this solution highly unpractical over time. As an alternative, our choice
725 of a custom UAV platform adopted in 2016 should ease a low cost switch to an RTK navigation system,
726 reducing the number of GCPs necessary for geo-referencing. While fixed-wing UAVs outperform
727 multicopters in terms of area covered and aircraft stability, the adaptability of our quadcopter platform,
728 together with the flexibility of terrestrial photogrammetric surveys might eventually enable continuous
729 monitoring of the Forni glacier and the provision of rapid hazard detection services for mountain guides
730 and the tourism sector in Stelvio National Park.

731 **Competing interests**

732 The authors declare that they have no conflict of interest.

733 **Acknowledgements**

734 This study was funded by DARAS, the department for autonomies and regional affairs of the presidency
735 of the council of the Italian government. The authors acknowledge the central scientific committee of
736 CAI (Club Alpino Italiano – Italian Alpine Club) and Levissima San Pellegrino S.P.A. for funding the
737 UAV quadcopter. The authors also thank Stelvio Park Authority for the logistic support and for
738 permitting the UAV surveys and IIT Regione Lombardia for the provision of the 2007 DEM.



739 Acknowledgements also go to the GICARUS lab of Politecnico Milano at Lecco Campus for providing
740 the survey equipment. Finally, the authors would also like to thank Tullio Feifer, Livio Piatta, and Andrea
741 Grossoni for their help during field operations.

742 **References**

743 Auer, I., Böhm, R., Lipa, W., Orlik, A., Potzmann, R., Schöner, W., Ungersböck, M., Matulla, C., Briffa,
744 K., Jones, P., Efthymiadis, D., Brunetti, M., Nanni, T., Maugeri, M., Mercalli, L., Mestre, O., Moisselin,
745 J.-M., Begert, M., Müller-Westermeier, G., Kveton, V., Bochnicek, O., Stastny, P., Lapin, M., Szalai, S.,
746 Szentimrey, T., Cegnar, T., Dolinar, M., Gajic-Capka, M., Zaninovic, K., Majstorovic, Z. and Nieplova,
747 E.: HISTALP - Historical instrumental climatological surface time series of the Greater Alpine Region,
748 *International Journal of Climatology*, 27, 17-46, 2007.

749 Azzoni, R.S., Senese, A., Zerboni, A., Maugeri, M., Smiraglia, C. and Diolauti, G.A.: Estimating ice
750 albedo from fine debris cover quantified by a semi-automatic method: the case study of Forni Glacier,
751 *Italian Alps*, *The Cryosphere*, 10, 665-679, doi:10.5194/tc-10-665-2016, 2016.

752 Azzoni, R.S., Fugazza, D., Zerboni, A., Senese, A., D'Agata, C., Maragno, M., Carzaniga, A.,
753 Cernuschi, M. and Diolauti, G.A.: The evolution of debris mantling glaciers in the Stelvio Park (Italian
754 Alps) over the time window 2003-2012 from high-resolution remote-sensing data, under revision in
755 *Progress in Physical Geography*.

756 Azzoni, R.S., Fugazza, D., Zennaro, M., Zucali, M., D'Agata, C., Maragno, D., Cernuschi, M.,
757 Smiraglia, C. and Diolauti, G.A.: Recent structural evolution of Forni Glacier tongue (Ortles-Cevedale
758 Group, Central Italian Alps), submitted to *Journal of Maps*.

759 Barazzetti L., Remondino F., Scaioni M. and Brumana R.: Fully Automatic UAV Image-Based Sensor
760 Orientation, In: Proc. ISPRS Comm. I Symp. 'Image Data Acquisition – Sensors & Platforms', Calgary
761 (Alberta-Canada), 16-18 Jun, *Int. Arch. Photogramm. Remote Sens. Spatial Inf. Sci.*, Vol. XXXVIII,
762 Part 1, 6 pp, 2010.

763 Barazzetti L., Forlani G., Remondino, F., Roncella R. and Scaioni M.: Experiences and achievements
764 in automated image sequence orientation for close-range photogrammetric projects, In: Proc. Int. Conf.
765 'Videometrics, Range Imaging, and Applications XI', 23-26 May, Munich (Germany), *Proc. of SPIE*,
766 Vol. 8085 (F. Remondino, M.R. Shortis, Eds.), paper No. 80850F, 13 pp. (e-doc), DOI:
767 10.1117/12.890116, 2011.

768 Berthier, E., Arnaud, Y., Kumar, R., Ahmad, S., Wagnon, P. and Chevallier, P.: Remote sensing
769 estimates of glacier mass balances in the Himachal Pradesh (Western Himalaya, India), *Remote
770 sensing of environment*, 108, 327-338, 2007.

771 Bhardwaj, A., Sam, L., Akanksha, Martin-Torres, F.J. and Kumar, R.: UAVs as remote sensing
772 platform in glaciology: Present applications and future prospects, *Remote sensing of environment*, 175,
773 196-204, 2016a.



- 774 Bhardwaj, A., Sam, L., Bhardwaj, A. and Martín-Torres, F.J.: LiDAR remote sensing of the cryosphere:
775 Present applications and future prospects, *Remote Sensing of Environment*, 177, 125-143, 2016b.
- 776 Blaschke, T.: Object based image analysis for remote sensing. *ISPRS J. Photogramm. Remote Sens.*
777 65, 2–16, 2010.
- 778 Blasone G., Cavalli M. and Cazorzi F.: Debris-Flow Monitoring and Geomorphic Change Detection
779 Combining Laser Scanning and Fast Photogrammetric Surveys in the Moscardo Catchment (Eastern
780 Italian Alps). In: Lollino G., Arattano M., Rinaldi M., Giustolisi O., Marechal JC., Grant G. (eds)
781 Engineering Geology for Society and Territory - Volume 3. Springer, Cham. doi: 10.1007/978-3-319-
782 09054-2_10, 2015
- 783 Bocchiola, D. and Diolaiuti, G. Evidence of climate change within the Adamello Glacier of Italy,
784 *Theor. App. Climat.*, 100, 3-4, 351369, doi: 10.1007/s00704-009-0186-x, 2010.
- 785 Brunetti, M., Lentini, G., Maugeri, M., Nanni, T., Auer, I., Boehm, R. and Schoener, W.: Climate
786 variability and change in the Greater Alpine Region over the last two centuries based on multi-variable
787 analysis, *Int. J. Climatol*, 29,2197-2225, doi: 10.1002/joc.1857, 2009
- 788 Citterio, M., Diolaiuti, G., Smiraglia, C., Verza, G.p. and Meraldi, E.: Initial results from the Automatic
789 Weather Station (AWS) on the ablation tongue of Forni Glacier (Upper Valtellina, Italy) . *Geografia*
790 *Fisica e Dinamica Quaternaria*, 141-151, 2007.
- 791 Colomina, I. and Molina, P.: Unmanned aerial systems for photogrammetry and remote sensing: A
792 review, *ISPRS Journal of Photogrammetry and Remote Sensing*, 92, 79-97, 2014.
- 793 D'Agata, C., Bocchiola, D., Maragno, D., Smiraglia, C. and Diolaiuti, G.A.: Glacier shrinkage driven
794 by climate change during half a century (1954–2007) in the Ortles-Cevedale group (Stelvio National
795 Park, Lombardy, Italian Alps), *Theor Appl Climatol*, 116, 169-190, 2014.
- 796 Dall'Asta, E., Forlani, G., Roncella, R., Santise, M., Diotri, F. and Morra di Cella, U.: Unmanned Aerial
797 Systems and DSM matching for rock glacier monitoring, *ISPRS Journal of Photogrammetry and Remote*
798 *Sensing*, available online at www.sciencedirect.com/science/journal/aip/09242716, last access: 29 January
799 2017, 2017.
- 800 Diolaiuti, G.A. and Smiraglia, C.: Changing glaciers in a changing climate: how vanishing
801 geomorphosites have been driving deep changes in mountain landscapes and environments,
802 *Géomorphologie : relief, processus, environnement*, 2, 131-152, 2010.
- 803 Diolaiuti, G.A., Bocchiola, D., D'Agata, C. and Smiraglia, C.: Evidence of climate change impact upon
804 glaciers' recession within the Italian Alps, *Theor. Appl. Climatol.*, 109,429-445, DOI 10.1007/s00704-
805 012-0589-y, 2012
- 806 Eltner, A., Kaiser, A., Castillo, C., Rock, G., Neugirg, F. and Abellán, A.: Image-based surface
807 reconstruction in geomorphometry – merits, limits and developments. *Earth Surface Dynamics*, 4, 359-
808 389, doi: 10.5194/esurf-4-359-2016, 2016.



- 809 Fioletti, M., Bonetti, M., Smiraglia, C., Diolaiuti, G.A., Breganze, C., dal Toso, M. and Facco, L.:
810 Indagini radar per lo studio delle caratteristiche endoglaciali del ghiacciaio dei Forni in alta Valtellina,
811 Neve e Valanghe, 87, 40-45, 2016
- 812 Fischer, M., Huss, M., Barboux, C. and Hoelzle, M.: The new Swiss Glacier Inventory SGI2010:
813 relevance of using high-resolution source data in areas dominated by very small glaciers, Arctic Antarctic
814 and Alpine Research, 46,933-945, 2014.
- 815 Fonstad, M.A., Dietrich, J.T., Courville, B.C., Jensen, J.L. and Carbonneau, P.E.: Topographic structure
816 from motion: a new development in photogrammetric measurement, Earth Surface Processes and
817 Landforms, 38, 421-430, 2013.
- 818 Fugazza, D., Senese, A., Azzoni, R.S., Smiraglia, C., Cernuschi, M., Severi, D. and Diolaiuti, G.A.:
819 High-resolution mapping of glacier surface features. The UAV survey of the Forni glacier (Stelvio
820 national park, Italy), Geogr. Fis. Dinam. Quat, 38, 25-33, DOI 10.4461/GFDQ.2015.38.03, 2015.
- 821 Fugazza, D., Senese, A., Azzoni, R.S., Maugeri, M. and Diolaiuti, G.A.: Spatial distribution of surface
822 albedo at the Forni Glacier (Stelvio National Park, Central Italian Alps), Cold Regions Science and
823 Technology, 125, 128-137, 2016.
- 824 Garavaglia, V., Diolaiuti, G.A., Smiraglia, C., Pasquale, V. and Pelfini, M.: Evaluating Tourist
825 Perception of Environmental Changes as a Contribution to Managing Natural Resources in Glacierized
826 areas: A Case Study of the Forni Glacier (Stelvio National Park, Italian Alps), Environmental
827 management, 50, 1125-1138, 2012.
- 828 Garambois, S., Legchenko, A., Vincent, C. and Thibert, E.: Ground-penetrating radar and surface nuclear
829 magnetic resonance monitoring of an englacial water-filled cavity in the polythermal glacier of Tête
830 Rousse, Geophysics, 81, 131-146, 10.1190/GEO2015-0125.1, 2016.
- 831 Gardent, M., Rabatel, A., Dedieu, J.-P., Deline, P.: Multitemporal glacier inventory of the French Alps
832 from the late 1960s to the late 2000s, Global and planetary change, 120, 24-37, 2014.
- 833 Gindraux, S., Boesch, R. and Farinotti, D.: Accuracy Assessment of Digital Surface Models from
834 Unmanned Aerial Vehicles' Imagery on Glaciers, Remote sensing, 9, 186, 2-15, doi:10.3390/rs9020186,
835 2017
- 836 Giussani, A. and Scaioni, M.: Application of TLS to Support Landslides Study: Survey Planning,
837 Operational Issues and Data Processing. In: Proc. Int. Work. 'Laserscanners for Forest and Landscape
838 Assessment – Natscan 2004,' Freiburg in B. (Germany), 3-6 October, *Int. Arch. Photogramm. Remote
839 Sens. Spatial Inf. Sci.*, Vol. XXXVI, Part 8/W2, 318-323, 2004.
- 840 Gobiet, A., Kotlarski, S., Beniston, M., Heinrich, G., Rajczak, J., Stoffel, M.: 21st century climate change
841 in the European Alps—A review, Science of the total environment, 493, 1138-1151, 2014.
- 842 Harris, C., Arenson, L.U., Christiansen, H.H., Etzelmueller, B., Frauenfelder, R., Gruber, S., Haeberli,
843 W., Hauck, C., Hoelzle, M., Humlum, O., Isaksen, K., Kaab, A., Kern-Luetsch, M., Lehning, M.,
844 Matsuoka, N., Murton, J.B., Noetzi, J., Phillips, M., Ross, N., Seppaelae, M., Springman, S.M. and



- 845 Vonder Muehll, D.: Permafrost and climate in Europe: Monitoring and modelling thermal,
846 geomorphological and geotechnical responses, *Earth-Science reviews*, 92, 117-171, 2009.
- 847 Hodson, A., Anesio, A.M., Ng, F., Watson, R., Quirk, J., Irvine-Fynn, T., Dye, A., Clark, C., McCloy,
848 P., Kohler, J. and Sattler, B.: A glacier respire: Quantifying the distribution and respiration CO₂ flux of
849 cryoconite across an entire Arctic supraglacial ecosystem, *Journal of Geophysical Research*, 112, 2007.
- 850 Hofmann-Wellenhof, B., Lichtenegger, H. and Wasle, E.: *GNSS – GPS, GLONASS, Galileo & more*,
851 Springer, 2008.
- 852 Howat, I.M., Smith, B.E., Joughin, I. and Scambos, T.A.: Rates of southeast Greenland ice volume loss
853 from combined ICESat and ASTER observations, *Geophysical research letters*, 35, L17505,
854 doi:10.1029/2008GL034496, 2008
- 855 Immerzeel, W.W., Kraaijenbrink, P.D.A., Shea, J.M., Shrestha, A.B., Pellicciotti, F., Bierkens, M.F.P.
856 and de Jong, S.M.: High-resolution monitoring of Himalayan glacier dynamics using unmanned aerial
857 vehicles, *Remote sensing of Environment*, 150,93-103, 2014.
- 858 Inoue, J., Curry, J.A., Maslanik, J.A.: Application of aerosondes to melt pond observations over arctic
859 sea ice, *Journal of atmospheric and oceanic technology*, <http://dx.doi.org/10.1175/2007JTECHA955.1>,
860 2007.
- 861 James, M.R. and Robson, S.: Straightforward reconstruction of 3-D surfaces and topography with a
862 camera: Accuracy and geoscience application. *J. Geophys. Res.*, 117, F03017, doi:
863 10.1029/2011JF002289, 2012.
- 864 Jokinen, O. and Geist T.: Accuracy aspects in topographical change detection of glacier surface, in:
865 *Remote sensing of glaciers*, CRC Press/Balkema, Leiden, the Netherlands, 269-283, 2010
- 866 Lindenbergh, R. and Pietrzyk, P.: Change detection and deformation analysis using static and mobile
867 laser scanning. *Appl. Geomat.*, 7, 65–74, 2015.
868
- 869 Kaab, A., Huggel, C., Fischer, L., Guex, S. Paul, F., Roer., I., Salzmann, N., Schlaefli, S., Schmutz, K.,
870 Schneider, D., Strozzi, T. and Weidmann, Y.: Remote sensing of glacier- and permafrost-related hazards
871 in high mountains: an overview, *Natural Hazards and Earth System Sciences*, 5, 527–554, 2005.
- 872 Keiler, M., Knight, J. and Harrison, S.: Climate change and geomorphological hazards in the eastern
873 European Alps, *Phil. Trans. R. Soc. A*, 368, 2461–2479, 2010.
- 874 Kraus, K.: *Photogrammetry - Vol. 2*, Dümmler Verlag, Bonn, 1997.
- 875 Luhmann, T., Robson, S., Kyle, S. and Boehm, J.: *Close Range Photogrammetry: 3D Imaging*
876 *Techniques – 2nd Edition*, Walter De Gruyter Inc., Germany, 684 pages, 2014.
- 877 Mugnier, C.J.: Grids & Datum. Italian Republic. *Photogrammetric Engineering and Remote Sensing*,
878 71, 889-890, 2005.
- 879 Nuth, C. and Kaab, A.: Co-registration and bias corrections of satellite elevation data sets for quantifying
880 glacier thickness change, *The cryosphere*, 5, 271-290, 2011.



- 881 Osborne, M.: Mission planner software. <http://ardupilot.org/planner/>, last accessed (18/05/2017), 2013.
- 882 O'Connor, J., Smith, M.J. and James, M.R.: Cameras and settings for aerial surveys in the geosciences:
883 optimising image data, *Progress in Physical Geography*, 1-20, doi:
884 <https://doi.org/10.1177/0309133317703092>, 2017.
- 885 Pepe, M., Fregonese, L. and Scaioni, M.: Planning airborne photogrammetric and remote sensing
886 missions with modern platforms and sensors, Submitted to the *European Journal of Remote Sensing*,
887 2017.
- 888 Piermattei, L., Carturan, L. and Guarnieri, A.: Use of terrestrial photogrammetry based on structure
889 from motion for mass balance estimation of a small glacier in the Italian Alps. *Earth Surf. Proc. Land.*,
890 40, 1791-1802, doi: 10.1002/esp.3756, 2015.
- 891 Piermattei, L., Carturan, L., de Blasi, F., Tarolli, P., Dalla Fontana, G., Vettore, A. and Pfeifer, N.:
892 Suitability of ground-based SfM-MVS for monitoring glacial and periglacial processes, *Earth Surface*
893 *Dynamics*, 4, 325-443, doi: 10.5194/esurf-4-425-2016, 2016.
- 894 Pomerleau, F., Colas, F., Siegwart, R., & Magnenat, S.: Comparing ICP variants on realworld
895 data sets. *Autonomous Robots*, 34, 133–148, 2013.
- 896 Remondino, F., Barazzetti, L., Nex, F., Scaioni, M. and Sarazzi, D.: UAV Photogrammetry for
897 mapping and 3D modeling – Current status and future perspectives. In: Proc. Int. Conf. ‘Unmanned
898 Aerial Vehicle in Geomatics (UAV-g)’, Zurich (Switzerland), 14-16 Sept., *Int. Arch. Photogramm.*
899 *Remote Sens. Spatial Inf. Sci.*, Vol. XXXVIII, Part 1/C22A, 7 pages, 2014.
- 900 Remondino, F., Spera, M.G., Nocerino, E., Menna, F. and Nex, F.: State of the art in high density
901 image matching, *Photogramm. Rec.*, 29, 144-166, doi: 10.1111/phor.12063, 2014.
- 902 Reynolds Geo Sciences Ltd: Development of glacial hazard and risk minimisation protocols in rural
903 environments, available online at:
904 http://www.geologyuk.co.uk/mountain_hazards_group/pdf/Chapters_1_4.pdf, last accessed 30 May
905 2017, 2003.
- 906 Riccardi, A. Vassena, G., Scotti, R., Sgrenzaroli, M.: Recent evolution of the punta S.Matteo serac
907 (Ortles-Cevedale Group, Italian Alps), *Geogr. Fis, Dinam. Quat.*, 33, 215-219, 2010.
- 908 Rippin, D.M., Pomfret, A. and King, N.: High resolution mapping of supra-glacial drainage pathways
909 reveals link between micro-channel drainage density, surface roughness and surface reflectance, *Earth.*
910 *Surf. Process. Landforms*, 40, 1279-1290, doi: 10.1002/esp.3719, 2015.
- 911 Santise, M.: UAS photogrammetric blocks: accuracy, georeferencing and control. PhD thesis.
912 University of Parma, 2016.
- 913 Scaioni M., Giussani A., Roncoroni F., Sgrenzaroli M. and Vassena G.: Monitoring of Geological Sites by
914 Laser Scanning Techniques, *Int. Arch. Photogramm. Remote Sens. Spatial Inf. Sci.*, 35, 708-713, 2004.
- 915 Scaioni, M., Feng, T., Lu, P., Qiao, G., Tong, X., Li, R., Barazzetti, L., Previtali, M. and Roncella, R.:
916 Close-Range Photogrammetric Techniques for Deformation Measurement: Applications to Landslides,



- 917 In: M. Scaioni (Ed.), *Modern Technologies for Landslide Monitoring and Prediction*, Springer Berlin
918 Heidelberg, Germany, 13-41, DOI: 10.1007/978-3-662-45931-7_2, 2015.
- 919 Schofield, W. and Breach, M.: *Engineering Surveying - 6th Edition*, Butterworth-Heinemann, 2007.
- 920 Senese, A., Diolaiuti, G.A., Mihalcea, C. and Smiraglia, C.: Energy and Mass Balance of Forni Glacier
921 (Stelvio National Park, Italian Alps) from a Four-Year Meteorological Data Record, *Arctic, Antarctic
922 and Alpine Research*, 44, 122-134, 2012.
- 923 Smiraglia, C.: The medial moraines of Ghiacciaio dei Forni, Valtellina, Italy: morphology and
924 sedimentology, *Journal of Glaciology*, 35, 81-84, 1989.
- 925 Smiraglia, C., Azzoni, R.S., D'Agata, C., Maragno, D., Fugazza, D. and Diolaiuti, G.A.: The evolution
926 of the Italian glaciers from the previous data base to the new Italian inventory. preliminary considerations
927 and results, *Geogr. Fis. Dinam. Quat.*, 38, 79-87, DOI 10.4461/GFDQ.2015.38.08, 2015.
- 928 Smith, M.W., Carriwick, J.L. and Quincey, D.: Structure from motion photogrammetry in physical
929 geography. *Prog. Phys. Geog.*, 1-29, doi: 10.1177/0309133315615805, 2015.
- 930 Teunissen, P.J.G.: *Testing theory. An introduction. Series on Mathematical Geodesy and Positioning*,
931 VSSD Delft, The Netherlands, 2009.
- 932 United Nations Environmental Program: GEO-6, *Regional Assessment for the Pan-European Region*,
933 available on line at:
934 [http://www.unep.org/geo/sites/unep.org/geo/files/documents/unep_geo_regional_assessments_europe_
935 16-07513_hires.pdf](http://www.unep.org/geo/sites/unep.org/geo/files/documents/unep_geo_regional_assessments_europe_16-07513_hires.pdf), last accessed 29 May 2017, 2016.
- 936 Vincent, C., Thibert, E., Harter, M., Soruco, A. and Gilbert, A.: Volume and frequency of ice avalanches
937 from Tacconnaz hanging glacier, French Alps, *Annals of Glaciology*, 56, 17-25, doi:
938 10.3189/2015AoG70A017, 2015.
- 939 Vosselman, G. and Maas, H.G.: *Airborne and Terrestrial Laser Scanning*, Taylor & Francis Group, Boca
940 Raton, FL-USA, 2010.
- 941 Wang, S., Qin, D. and Xiao, C.: Moraine-dammed lake distribution and outburst flood risk in the Chinese
942 Himalaya, *Journal of Glaciology*, 61, 115-126, doi: 10.3189/2015JoG14J097, 2015.
- 943 Westoby, M.J., Brasington, J., Glasser, N.F., Hambrey, M.J. and Reynolds, J.M.: Structure-from-Motion'
944 photogrammetry: A low-cost, effective tool for geoscience applications, *Geomorphology*, 179: 300-314,
945 2012.
- 946 Zhang, X., Qiao, G. and Scaioni, M.: Evaluation of 3D reconstruction accuracy in the case of stereo
947 camera-pose configuration. In printing in: M. Barbarella, R. Cefalo and J. Zielinski (Ed.'s), *New
948 Advanced GNSS and 3D Spatial Techniques*, Lecture notes in Geoinformation and Cartography, Vol.
949 7418, Springer Verlag, Germany, 11 pages, 2017.
- 950



951 **Tables**

	2016 Survey	2014 Survey
Aircraft type	Quadcopter	Fixed wing
Commercial name	Customized, with Tarot frame 650 size, VR Brain 5.2 Autopilot & APM Arducopter 3.2.1 Firmware	SwingletCam built by SenseFly
Digital camera	Canon Powershot ELPH 320 HS	Canon Ixus 127 HS
Camera technical features	16 Megapixel, focal length 4.3 mm	16 Megapixel, focal length 4.3 mm
GNSS antenna	GPS+GLONASS (Galileo compatible)	GPS only
Weight (incl. payload)	2.75 Kg	0.50 Kg
Battery time	20-25 minutes	30 minutes

952 *Table 1: Details of UAV platforms employed during the 2016 and 2014 surveys*

953



Block	#Images	Total #valid TPs	Mean # projections per TP	Mean/min # TP per image	Mean/max RMSE reprojection [pixel]	Point cloud # points	Mean GSD[cm]	# GCPs	RMSE on GCPs [cm]
<i>Terrestrial Photogrammetry (Glacier Terminus)</i>	134	59,157	5.6	2,455 / 744	0.30 / 0.73	27.1M	1.5	7	34.4
<i>UAV 2016</i>	288	38,506	6.7	892 / 115	0.21 / 0.31	75.2M	5.7	8	40.5
<i>UAV 2014</i>	85	76,856	4.4	3935 / 2231	0.17 / 0.19	55.7M	11.9	0	n.a.

954 *Table 2: Statistics of photogrammetric blocks (TP: tie points; GCP: ground control points; RMSE: root*
 955 *mean square error).*

956



DEM pair	Elevation differences without co-registration shifts ($\mu_{\Delta H} \pm \sigma_{\Delta H}$) [m]	Co-registration shifts		Elevation differences without co-registration shifts ($\mu_{\Delta H} \pm \sigma_{\Delta H}$) [m]
		X [m]	Y [m]	
2007-2014	1.96±2.60	1.11	-1.11	0.00±1.70
2007-2016	-0.43±3.48	2.44	-1.11	0.00±2.60
2014-2016	-2.92±3.21	-0.20	-1.30	0.00±2.22

957 *Table 3: Statistics of the elevation differences between DEM pairs before and after the application of*
 958 *co-registration shifts.*

959



Sample Window	Size of sample windows	#points in sample windows		
	Width x depth x height [m]	(i) UAV photogrammetry	(ii) Terrestrial photogrammetry	(iii) TLS
1	49 x 57 x 22	-	1984k	141k
2	43 x 42 x 13	76k	2175k	130k
3	45 x 11 x 14	43k	712k	25k
4	24 x 28 x 10	62k	557k	33k
5	55 x 72 x 18	406k	810k	-

960

961 *Table 4: Number of points in each sample window.*

962



Sample Window	Mean and standard deviation of point density [points/m ²]			Number of point above the lower 12.5% percentile		
	(i) UAV Photogrammetry	(ii) Terrestrial Photogramm.	(iii) TLS	(i)	(ii)	(iii)
1	-	1654±637	226±100	-	880	26
2	109±29	2297±708	391±217	61	881	0
3	103±27	1978±606	151±60	49	766	31
4	108±22	1384±530	141±69	62	324	2
5	141±22	485±227	-	97	31	-

963

964 *Table 5: Mean and standard deviation of point density computed in five sample windows on the Forni*
 965 *Glacier terminus.*

966



Sample Window	Means and Std. Dev.s of M3C2 distances [cm]			RMSE of M3C2 distances [cm]			
	Ref.	TLS	TLS	UAV Photogramm.	TLS	TLS	UAV Photogramm
	Slave	Terrestrial Photogramm.	UAV Photogramm.	Terrestrial Photogramm.	Terrestrial Photogramm	UAV Photogramm.	Terrestrial Photogramm
1		4.5±7.4	-	-	8.7	-	-
2		-1.1±10.5	14.8±34.7	-14.5±26.7	10.6	37.7	30.4
3		8.4±4.1	14.7±15.1	-8.5±18.9	9.4	21.1	20.7
4		2.8±5.3	9.4±22.2	-2.3±24.9	6.0	24.0	25.0
5		-	-	-8.5±25.3	-	-	26.7

967

968 *Table 6: Statistics on computed M3C2 distances.*

969



DEM pair	Glacier Area analysed [km ²]	Mean thickness change [m]	Mean thinning rates [ma ⁻¹]
2007-2014	1.03	-25.06 ± 1.70	-3.58 ± 0.24
2007-2016	0.46	-37.39 ± 2.60	-4.15 ± 0.29
2014-2016	0.32	-10.40 ± 2.22	-5.20 ± 1.11

970 *Table 7: Average thickness change and thinning rates from DEM differencing over the maximum glacier*
971 *areas for each DEM pair, and corresponding uncertainty.*

972



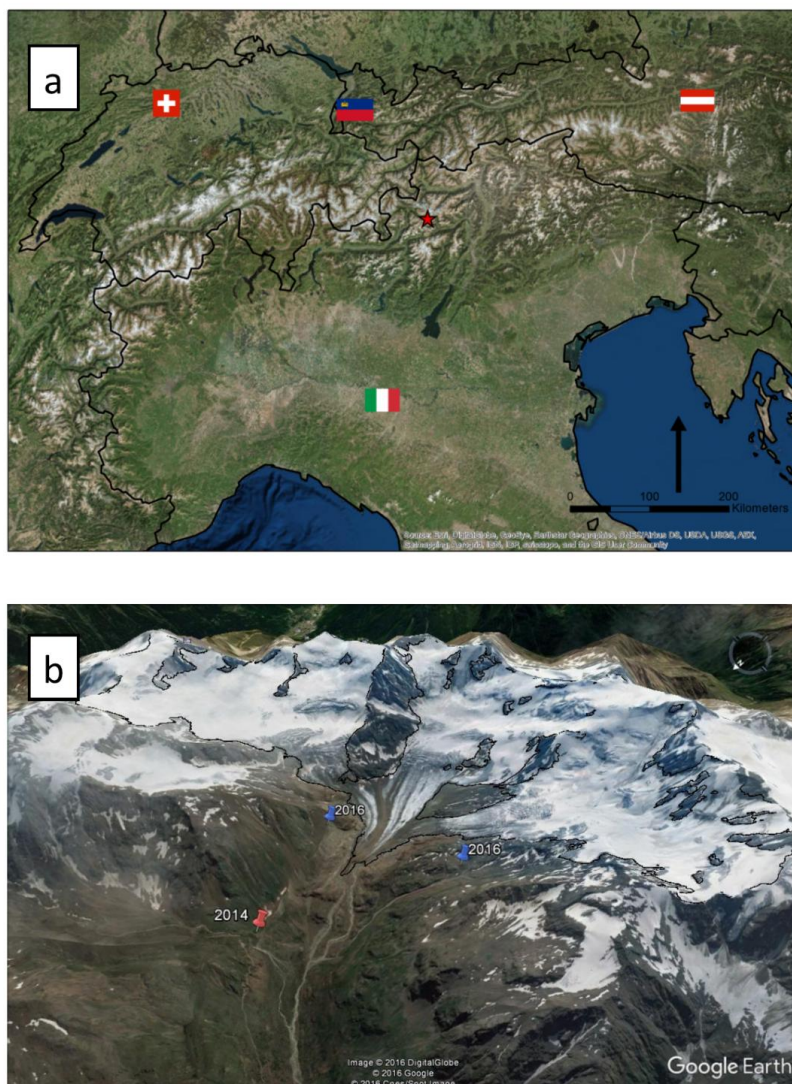
DEM pair	Mean thickness change [m]	Mean thinning rates [ma^{-1}]	Volume Change [10^6 m^3]
2007-2014	-31.91 ± 1.70	-4.55 ± 0.24	-10.00 ± 0.12
2007-2016	-42.86 ± 2.60	-4.76 ± 0.29	-13.46 ± 0.14
2014-2016	-10.41 ± 2.22	-5.20 ± 1.11	-3.29 ± 0.05

973 *Table 8: Average ice thickness change, thinning rates and volume loss from DEM differencing over a*
974 *common reference area of 0.32 km² for all DEM pairs. Uncertainty of thickness change expressed as 1 σ*
975 *of residual elevation differences over stable areas after DEM co-registration. See text for an explanation*
976 *of the uncertainty of volume changes.*

977

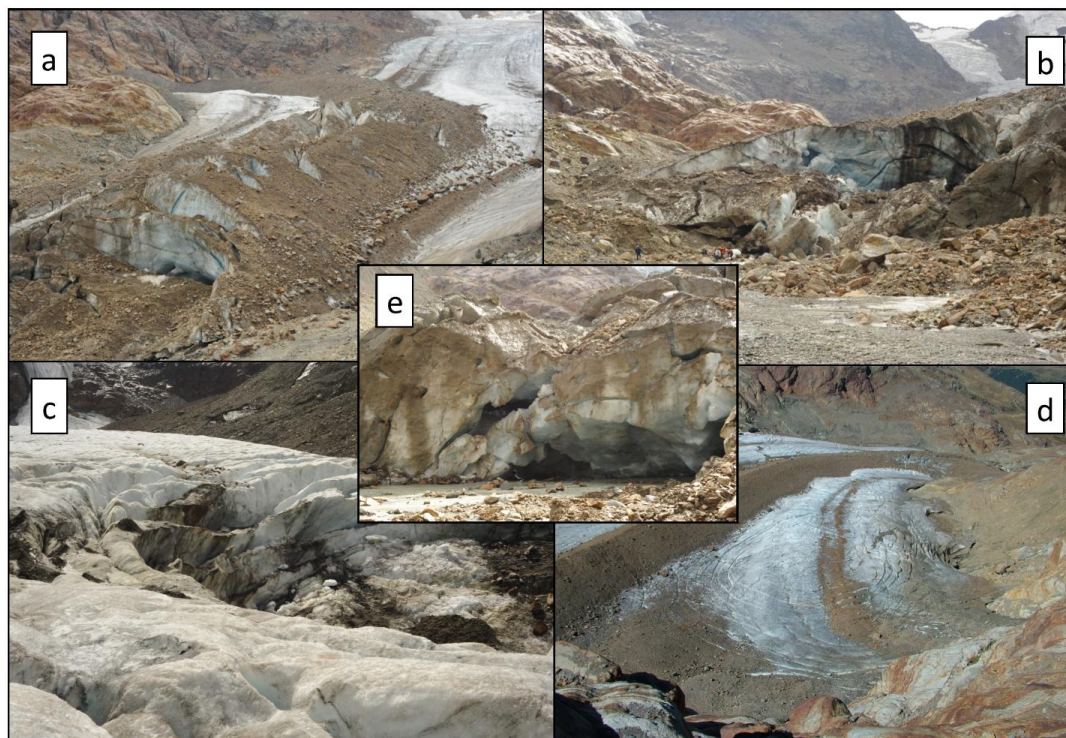


978 **Figures**
979



980
981
982
983
984
985

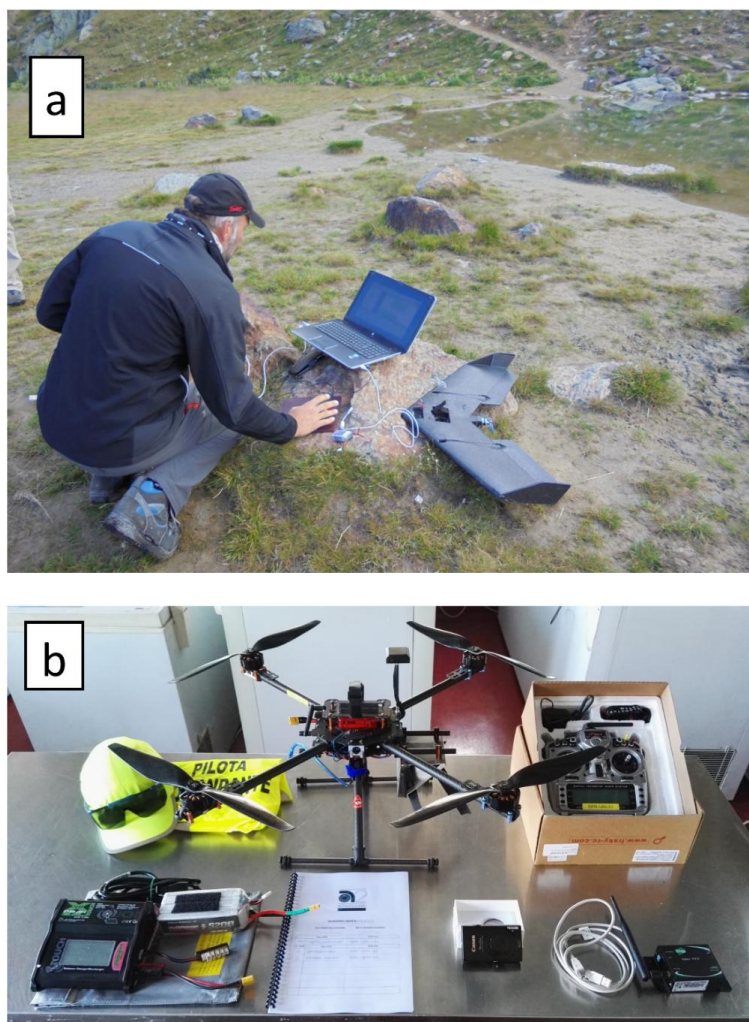
Figure 1: (a) Location of the Forni Glacier, marked with a red star, within Italy and the Central Alps. (b) Perspective view of the glacier and location of the take-off/landing sites for the 2014 and 2016 UAV surveys (in 2016 two different landing sites were used). Base maps courtesy of Bing Maps© and Google Earth©



986
987
988
989
990

Figure 2: Collapsing areas on the tongue of Forni Glacier. (a) Faults cutting across the eastern medial moraine; (b) glacier terminus; (c) Near-circular collapsed area on the central tongue; (d) Large ring fault on the eastern tongue at the base of the icefall. Photo courtesy of G.Cola; (e) Close-up of a vertical ice cliff at the glacier terminus.

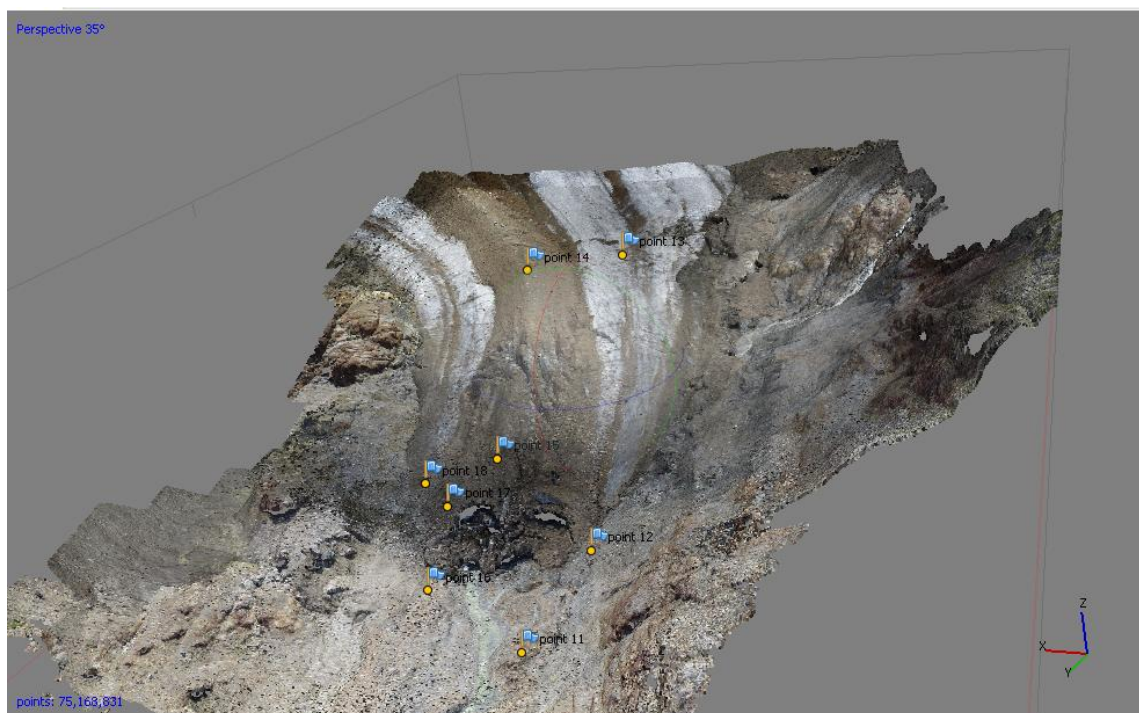
991



992

993 *Figure 3: The UAVs used in surveys of the Forni Glacier. (a) The SwingletCam fixed-wing aircraft*
994 *employed in 2014, at its take off site by Lake Rosole; (b) The quadcopter used in 2016 in the lab.*

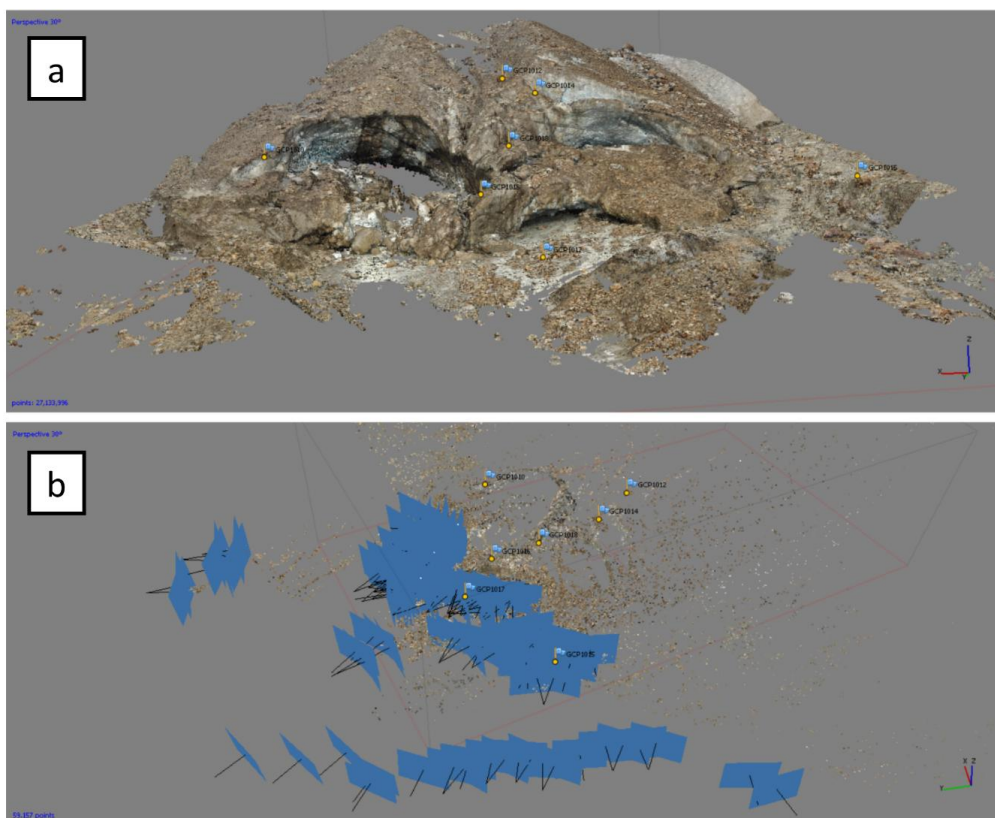
995



996

997 *Figure 4: Dense point cloud of the 2016 survey and location of the GCPs recorded with GNSS*
998 *equipment.*

999



1000

1001 *Figure 5: 3D reconstruction of the glacier terminus using terrestrial photogrammetry: (a) locations of*
1002 *camera stations in front of the glacier and 3D coordinates of tie points extracted during SfM for image*
1003 *orientation; (b) point clouds of the glacier terminus with positions of adopted GCPs.*

1004

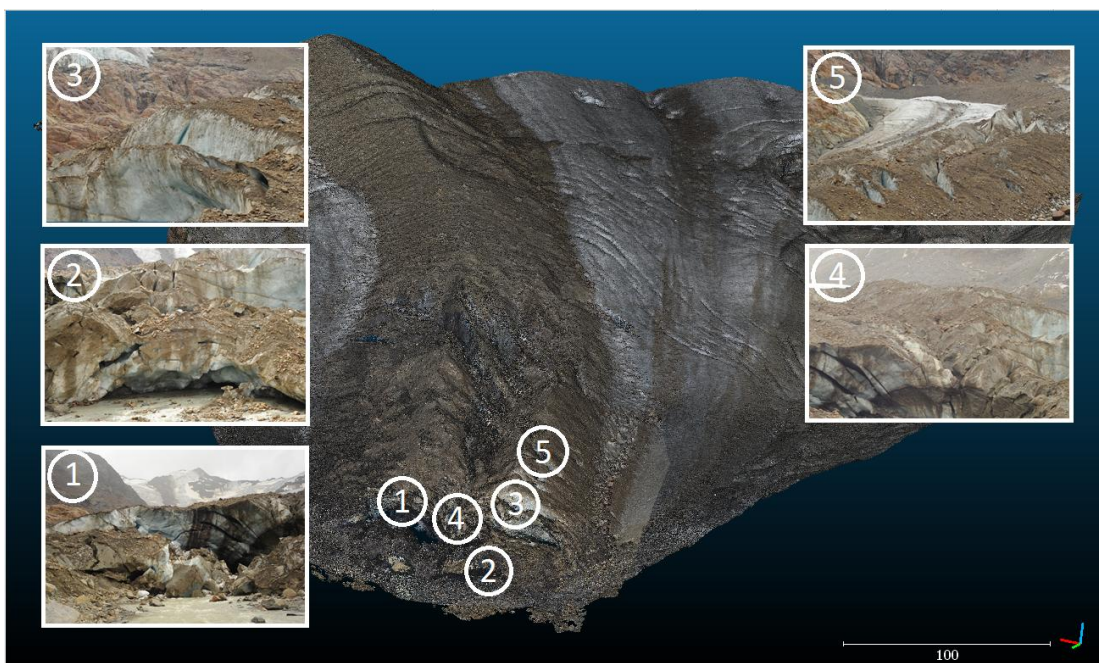


1005

1006 *Figure 6: survey operations of a GCP placed on a flat boulder on the proglacial plain of Forni Glacier.*

1007 *Photo courtesy of Livio Piatta*

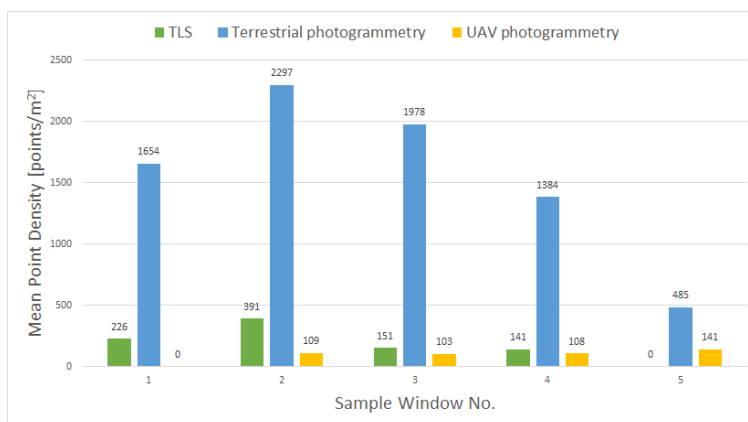
1008



1009

1010 *Figure 7: Sample windows on the glacier terminus area.*

1011



1012

1013 *Figure 8: Bar plot of mean point density computed in the five sample windows on the Forni Glacier*
1014 *terminus.*

1015

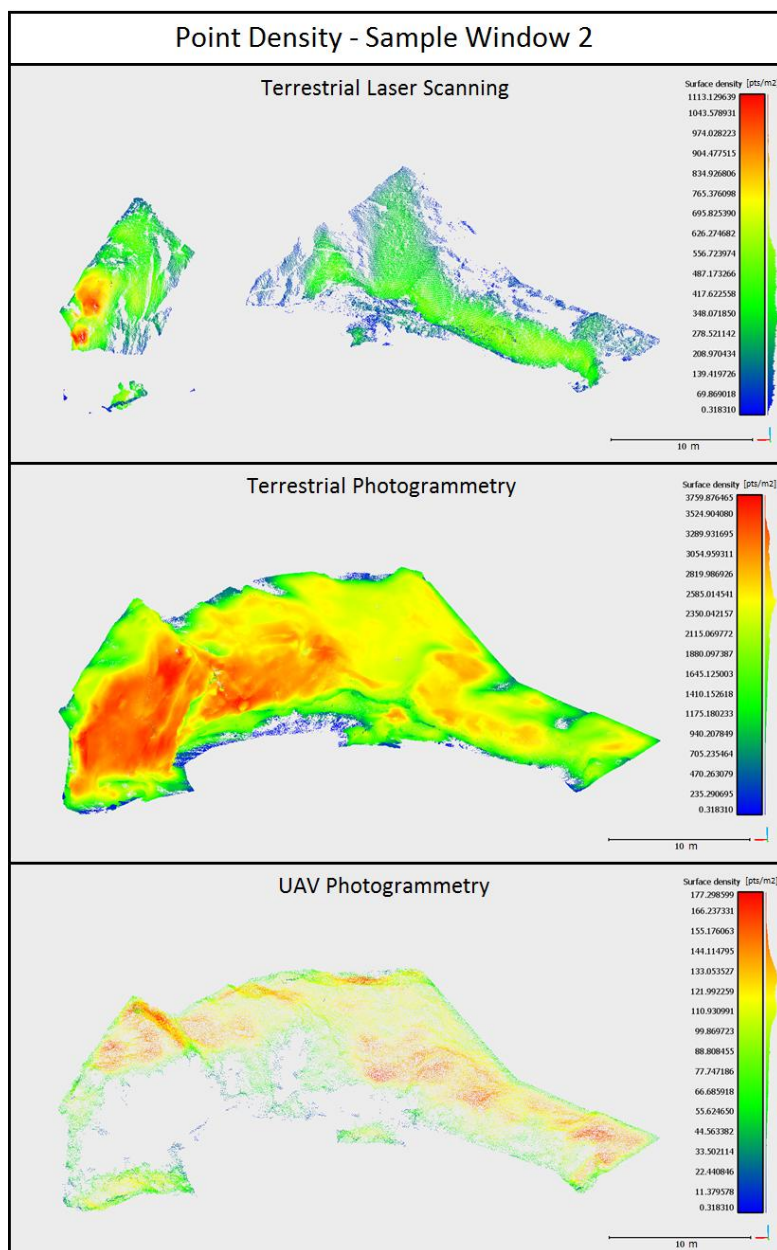


Figure 9: Maps of point density for Window 2.

1016
1017
1018

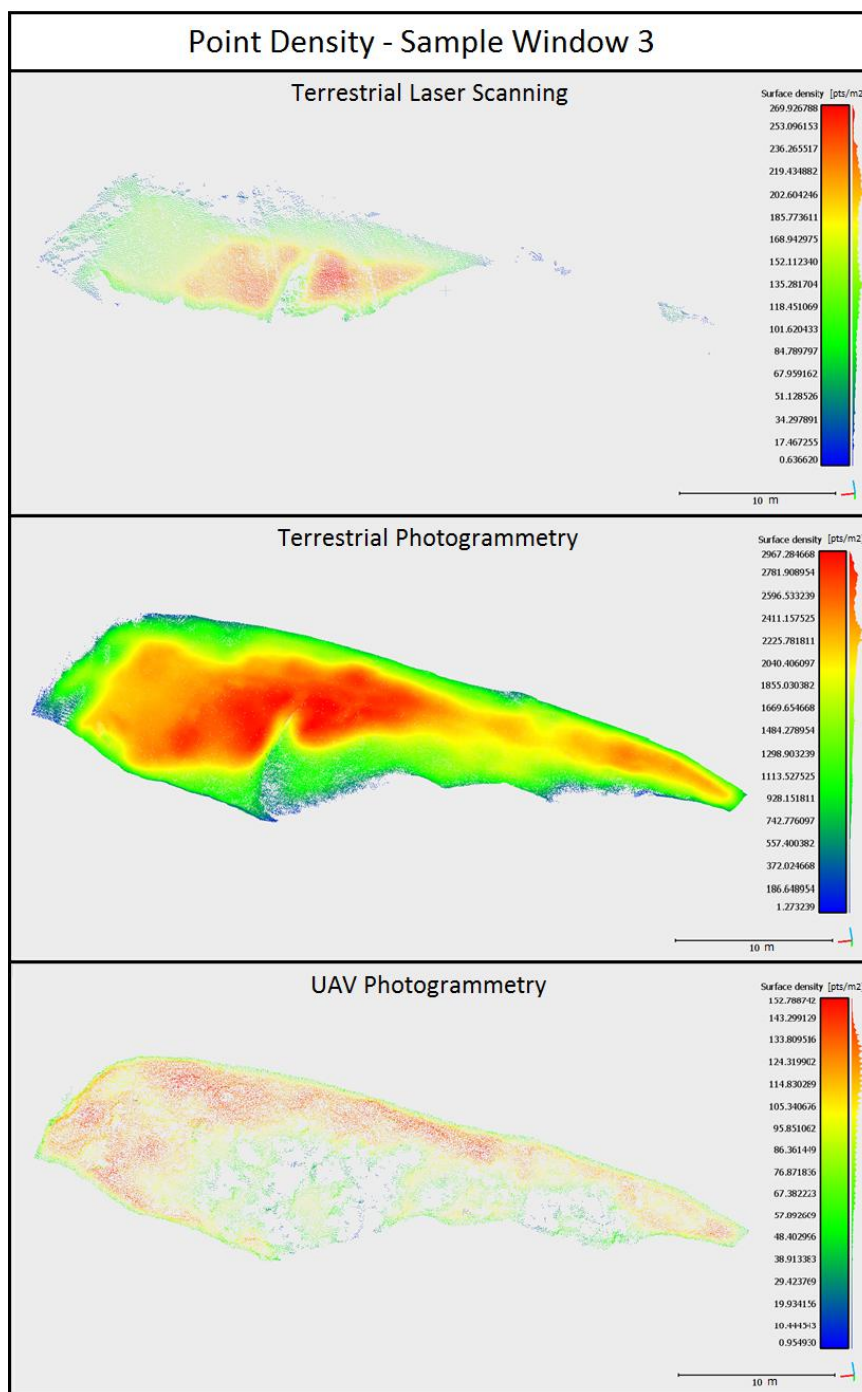
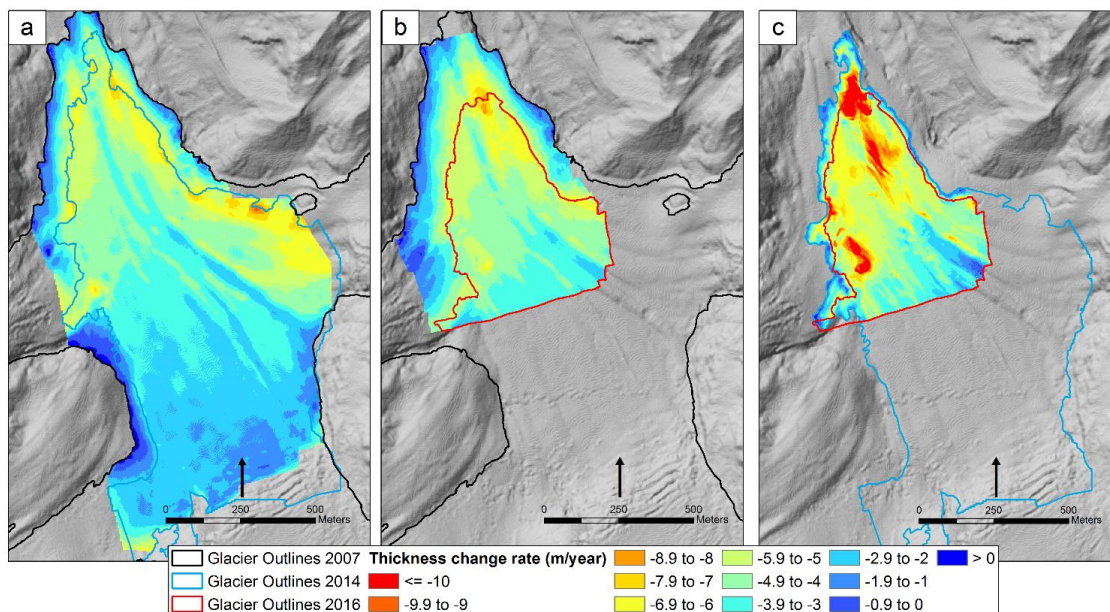


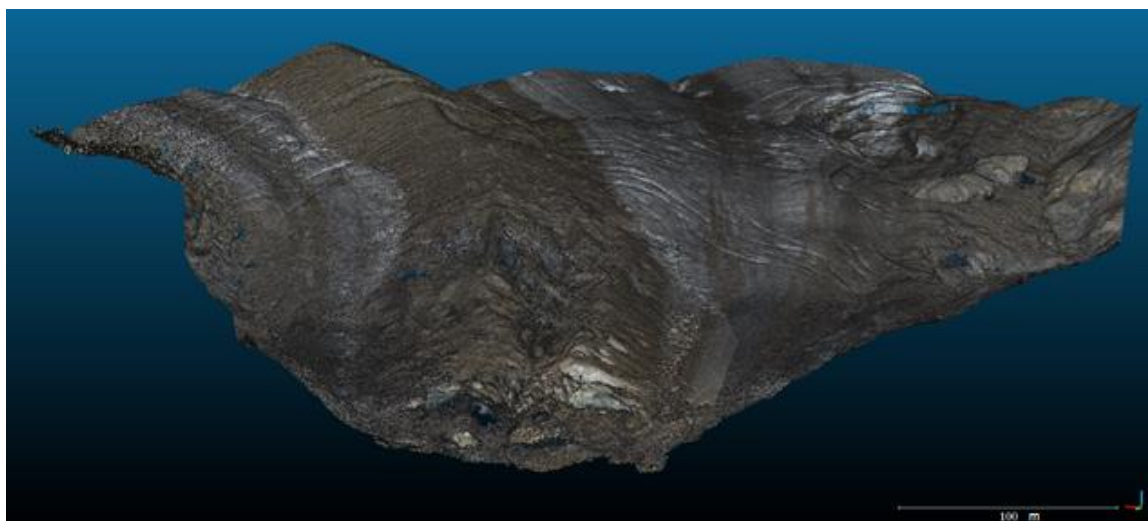
Figure 10: Maps of point density for Window 3.

1019
1020
1021



1022
 1023 *Figure 11: Ice thickness change rates from DEM differencing over (a) 2007-2014; (b) 2007-2016; (c)*
 1024 *2014-2016. Glacier outlines from 2014 and 2016 are limited to the area surveyed during the UAV*
 1025 *campaigns. Base map from hillshading of 2007 DEM.*

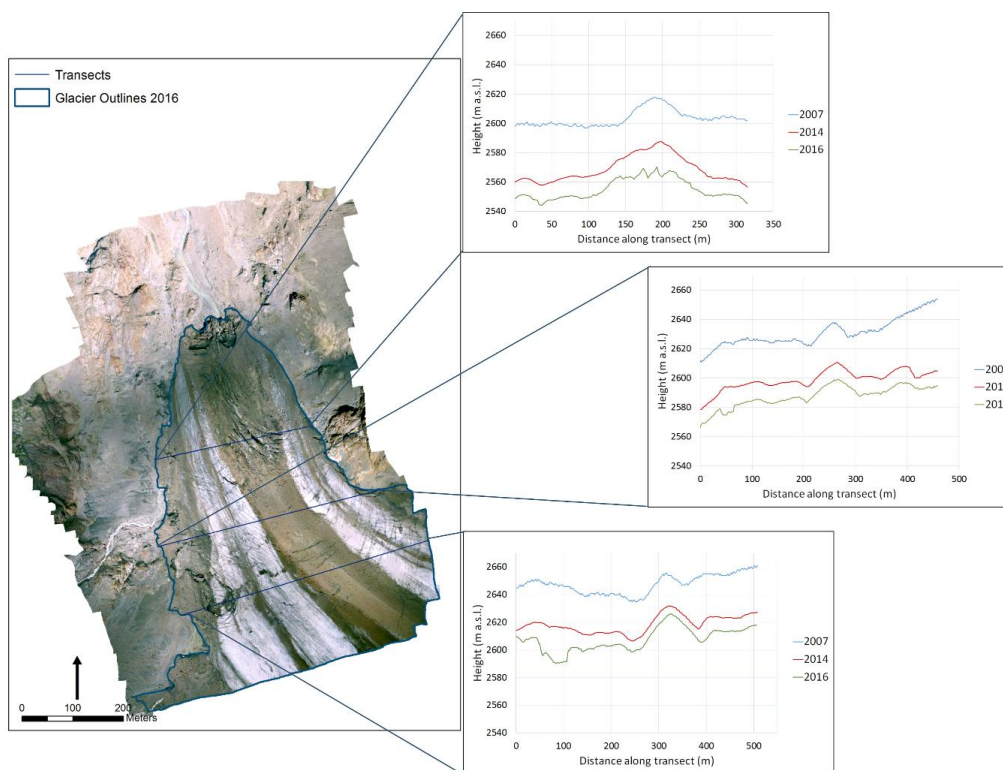
1026



1027

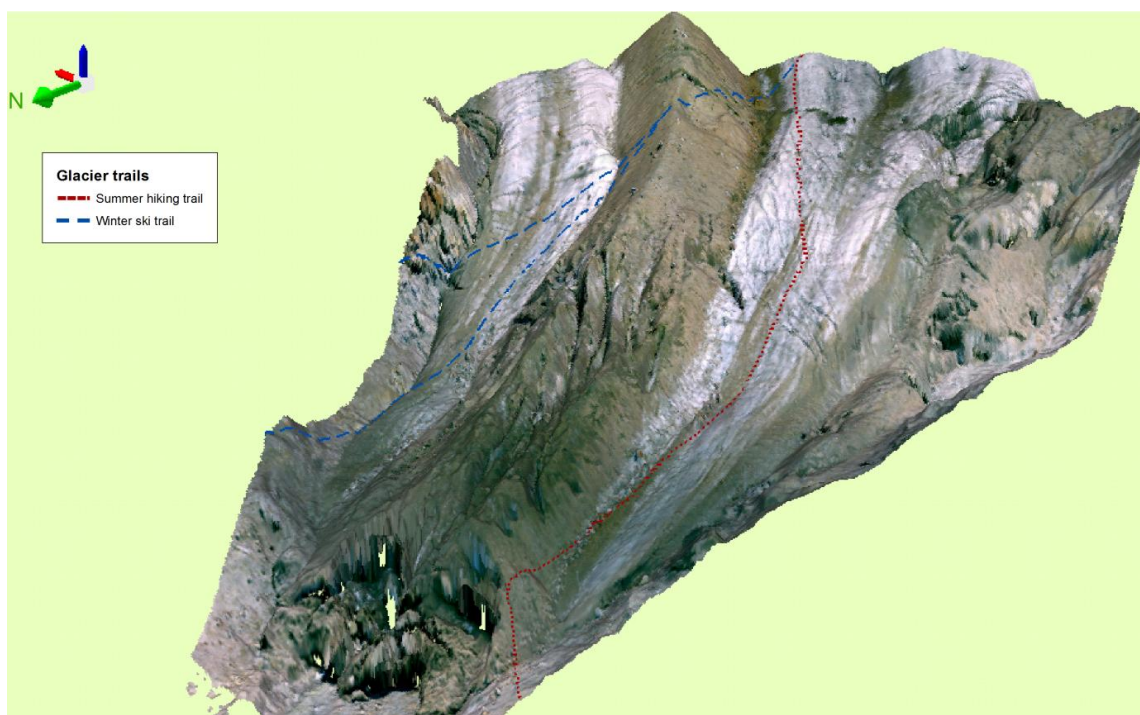
1028 *Figure 12: Merged 3D model of the Forni Glacier tongue, integrating points clouds derived from UAV*
1029 *and terrestrial photogrammetry, subsampled to keep a minimum distance between adjacent points of*
1030 *20 cm, and coloured with RGB information from images.*

1031



1032
1033 *Figure 13: Across-glacier transects of elevation of the ice surface in 2007, 2014 and 2016, based on*
1034 *the respective DEMs. Base map is the orthomosaic obtained from the 2016 UAV survey.*

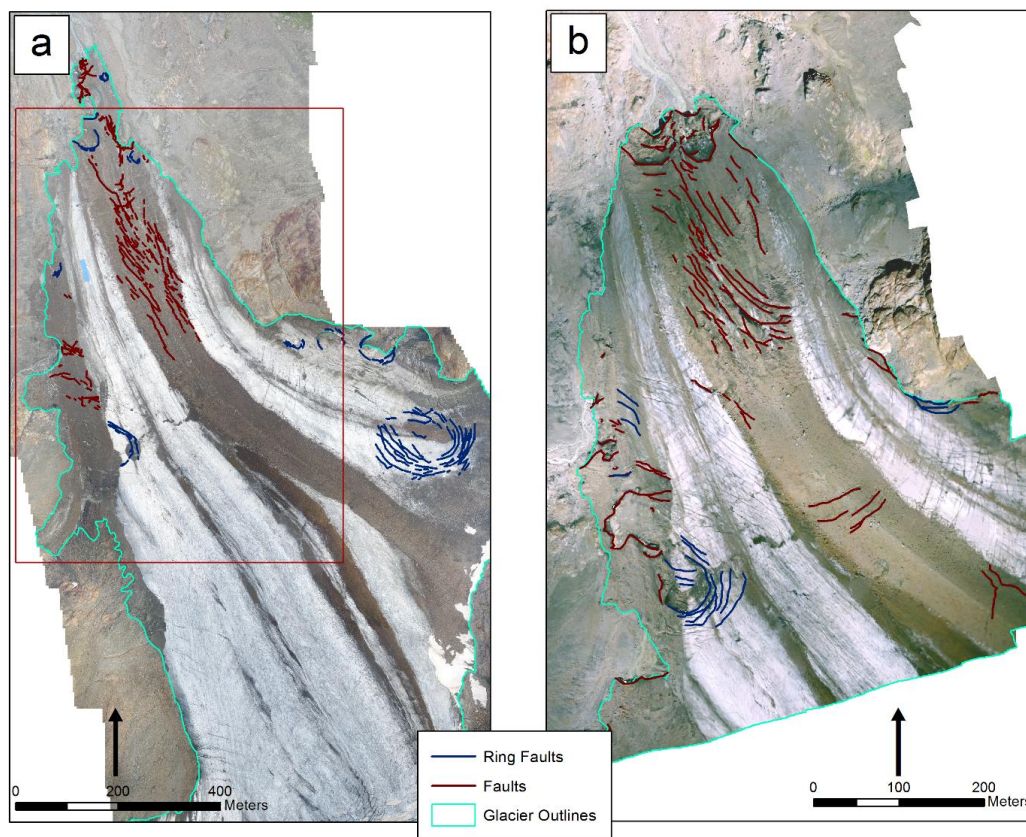
1035



1036

1037 *Figure 14: perspective view of the glacier tongue showing summer and winter trails crossing the*
1038 *glacier. Trails available from Kompass online cartography at [https://www.kompass-](https://www.kompass-italia.it/info/mappa-online/)*
1039 *italia.it/info/mappa-online/. Elevation surface is the merged point cloud obtained from UAV and close-*
1040 *range photogrammetry, with 2x vertical exaggeration.*

1041



1042

1043 *Figure 15: location of collapse structures on the Forni Glacier, shown on the respective UAV*

1044 *orthophoto. (a) 2014. The red box marks the area surveyed in 2016. (b) 2016.*